Supplementary Information for

Nonclassical growth of immiscible high-entropy materials

Yuanming Zhang[1, 2, 3†], Yang Li[1, 2†], Xiaoming Xu[1, 2], Yong Chen[1, 2], Zhonghua Li[1, 2], Xuexi Yan[4, 5], Zhigang Zou[1, 2], Cheng-Wei Qiu[3], Ghim Wei Ho[3, 6*], Zhaosheng Li[1, 2*]

[1]Collaborative Innovation Center of Advanced Microstructures, National Laboratory of Solid State Microstructures, College of Engineering and Applied Sciences, Nanjing University, Nanjing 210093, China
[2]Jiangsu Key Laboratory of Nano Technology, Nanjing University, Nanjing 210093, China
[3]Department of Electrical and Computer Engineering, National University of Singapore, Singapore 117583, Singapore
[4]Shenyang National Laboratory for Materials Science, Institute of Metal Research, Chinese Academy of Sciences, Shenyang 110016, China
[5]School of Materials Science and Engineering, University of Science and Technology of China, Shenyang 110016, China
[6]Department of Materials Science and Engineering, National University of Singapore, Singapore 117575, Singapore
*Corresponding Author. Email: elehgw@nus.edu.sg; zsli@nju.edu.cn
[†]These authors contributed equally to this work.

Supplementary note 1

Homogeneous nucleation:

The rate of homogeneous nucleation within the framework of classical nucleation is given by Gibbs-Thomson relationship[1]:

$$J = \beta Z C_0 \exp\left(-\frac{\Delta G^*}{kT}\right)$$

Here, J represents nucleation rate, β represents a kinetic pre-factor, Z represents Zendelovich factor, C_0 represents the equilibrium solute concentration, ΔG^* represents the height of the free-energy barrier.

Starting from the Gibbs-Thomson relationship, under a certain degree of supersaturation or undercooling, a crystal can exist and grow spontaneously only when its radius is larger than the critical radius. A crystal with a critical radius is called a nucleus. The reduction in Gibbs free energy caused by the transformation of individual atom or molecule in a metastable fluid phase into individual atom or molecule in a stable phase (crystal) is Δg. If the volume of atoms or molecules in the crystal is Ω_S and the interface between the crystal and the fluid can be γ_{SF}, then the change in Gibbs free energy caused by the formation of a spherical crystal with a radius r in the metastable fluid phase is[2, 3]:

$$\Delta G(r) = \left(\frac{\frac{4}{3}\pi r^3}{\Omega_S}\right)\Delta g + 4\pi r^2 \gamma_{SF}$$

$$\Delta G^* = \frac{16\pi \Omega_S^2 \gamma_{sf}^3}{3\Delta g^2}$$

$$r^* = \frac{2\gamma_{SF}\Omega_S}{\Delta g}$$

If a spherical crystal with a radius of r is a collection of i atoms or molecules:

$$\Delta G(i) = i \cdot \Delta g + A(i)\gamma_{SF}$$

For the surface area of polyhedral:

$$A(i) = \eta i^{\frac{2}{3}}$$

$$V(i) = i\Omega_S$$

If a polyhedron is a cube with side length a,

$$A = 6V^{\frac{2}{3}}$$

$$A(i) = 6\Omega_S^{\frac{2}{3}} i^{\frac{2}{3}}$$

$$\eta = 6\Omega_S^{\frac{2}{3}}$$

$$\eta = 36\pi^{\frac{1}{3}}\Omega_S^{\frac{2}{3}}$$

Heterogeneous nucleation:

Assuming the formation of the crown-shaped crystal nucleus, based on geometric derivation, the new formula becomes the following form (Supplementary Fig. 1):

$$\Delta G(r) = \left(\frac{\frac{4}{3}\pi r^3}{\Omega_S}\Delta g + 4\pi r^2 \gamma_{SF}\right)\left(\frac{2 - 3cos\theta + cos^3\theta}{4}\right) \quad \gamma_{SF} = \sigma_{\alpha L}$$

$$\Delta G^* = \frac{16\pi\Omega_S^2\gamma_{sf}^3}{3\Delta g^2} \times \left(\frac{2 - 3cos\theta + cos^3\theta}{4}\right)$$

$$r^* = \frac{2\gamma_{SF}\Omega_S}{\Delta g}$$

The growth rate:

$$G = k(S - 1)^g$$

Here, where k is the growth rate constant, it is a function of solubility and temperature, S represents the supersaturation, and g represents the growth order.

During the initial nucleation stage of diamond film growth, based on lattice mismatch and surface energy, three distinct growth modes can be observed (Supplementary Fig. 2). Frank–van der Merwe Mode (Layered Growth): In this mode, numerous two-dimensional crystal nuclei form on the substrate. These nuclei grow and connect to form a single atomic layer. Once the substrate is fully covered, the process repeats layer by layer, resulting in a continuous film of a certain thickness. Volmer–Weber Mode (Island Growth): This mode involves the formation of three-dimensional island-like crystal nuclei on the substrate. These nuclei continue to grow, eventually forming a polycrystalline film with a rough surface. Stranski-Krastanov Mode (Intermediate Growth): When there is significant lattice mismatch between the film material and the substrate, the strain energy increases as more atomic layers are deposited. To relieve this strain, the growth mode transitions from layered growth to island growth once the film reaches a critical thickness.

Yang's equations: $\sigma_{\beta L} = \sigma_{\alpha\beta} + \sigma_{\alpha L}\cos\theta$

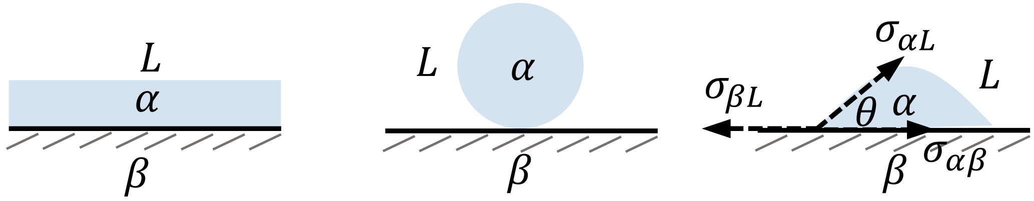

$\sigma_{\beta L} \geq \sigma_{\alpha\beta} + \sigma_{\alpha L}$

$\sigma_{\alpha\beta} - \sigma_{\alpha L} \geq \sigma_{\beta L} \geq 0$

$\sigma_{\alpha\beta} + \sigma_{\alpha L} \geq \sigma_{\beta L} \geq \sigma_{\alpha\beta} - \sigma_{\alpha L}$

Supplementary Fig. 1 Interface energy relationship of heterogeneous nucleation.

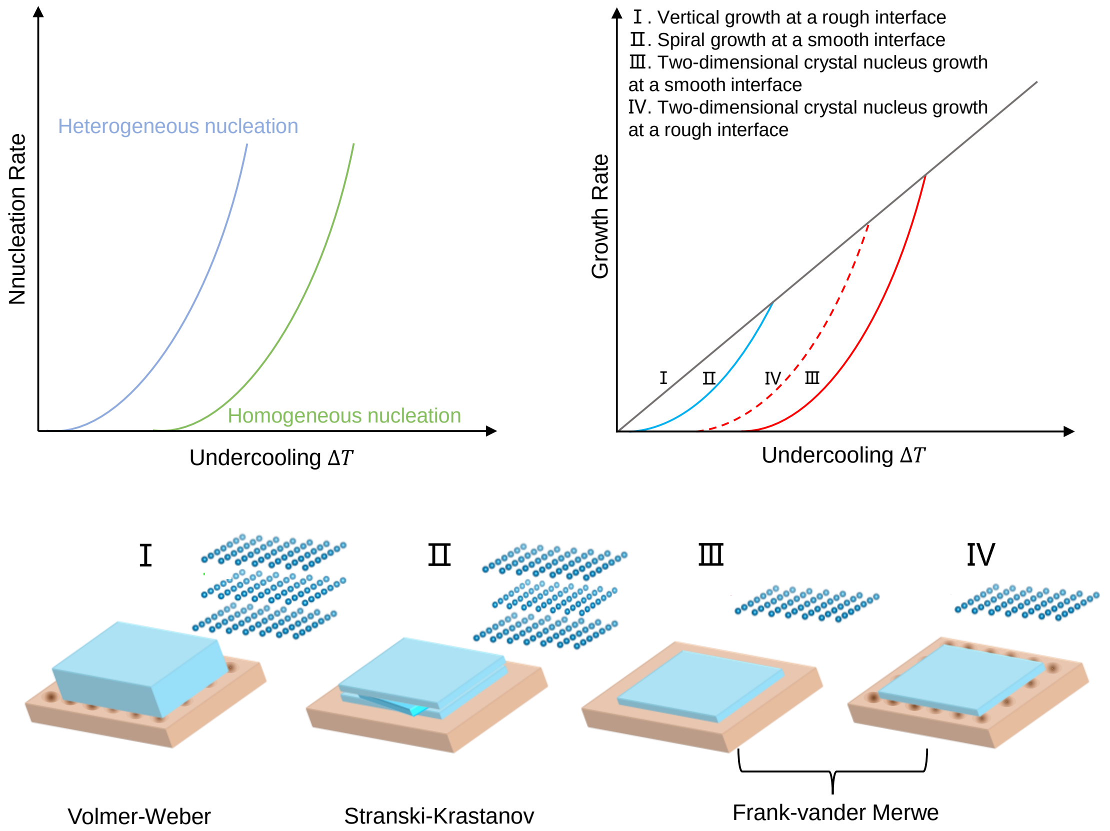

Supplementary Fig. 2 On-surface growth curves. Inspired by the growth model of diamond, where in-plane atomic attachment exhibits a layered structure rather than an island-like configuration[4–6].

Supplementary note 2

Meta-analysis of HEAs and their correlation with surface atomization processes:

HEAs, defined by the inclusion of five or more principal elements, offer a paradigm shift in materials science. Through comprehensive meta-analysis (Fig. 1a and Supplementary Figs. 3 and 4), we have established a quantitative relationship between the mixing enthalpy of binary alloys and other governing parameters for the first time. Our findings demonstrate a robust scaling relationship between the mixing enthalpy and the electronegativity difference as the number of constituent metallic elements increases. This scaling behavior provides critical insights into surface growth mechanisms.

Specifically, the heterogeneous atomization process on the substrate surface profoundly enhances the atomic coordination environment, modulating the electronegativity differential and influencing growth kinetics (Supplementary Fig. 5). Furthermore, metastable phase substrates, characterized by elevated surface energy, significantly suppress homogeneous nucleation rates at low temperatures. This suppression mitigates conventional monomer-by-monomer pathways, favoring a growth regime dominated by direct atomic attachment engineering (Supplementary Fig. 6). Such nonclassical growth pave the way for tailored material design, optimizing structural stability and functionality at the nanoscale.

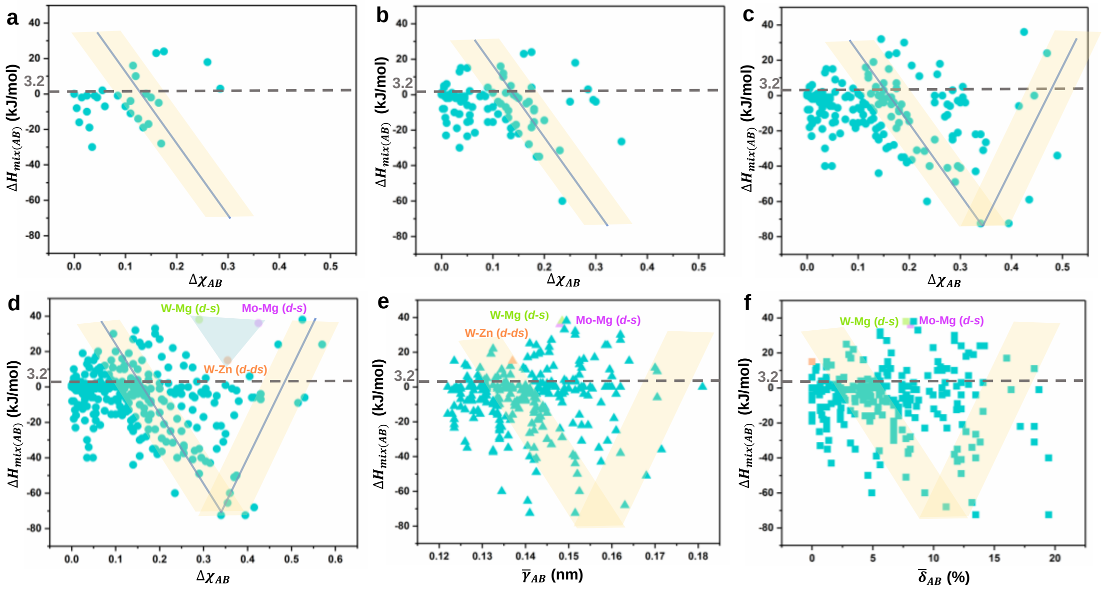

Supplementary Fig. 3 Meta-analysis of between mixing enthalpy and electronegativity difference and atomic radius from a dataset of metallic elements. **a**, Quantity of metal elements: 8. **b**, Quantity of metal elements: 13. **c**, Quantity of metal elements: 18. **d,** Quantity of metal elements: 23. The triangle region represents the transition zone of segmentation points. **e**, Meta-analysis of between mixed enthalpy and average atomic radius. No obvious scaling relationship can be revealed. **f**, Meta-analysis of between mixed enthalpy and atom radii difference factor. No obvious scaling relationship can be revealed.

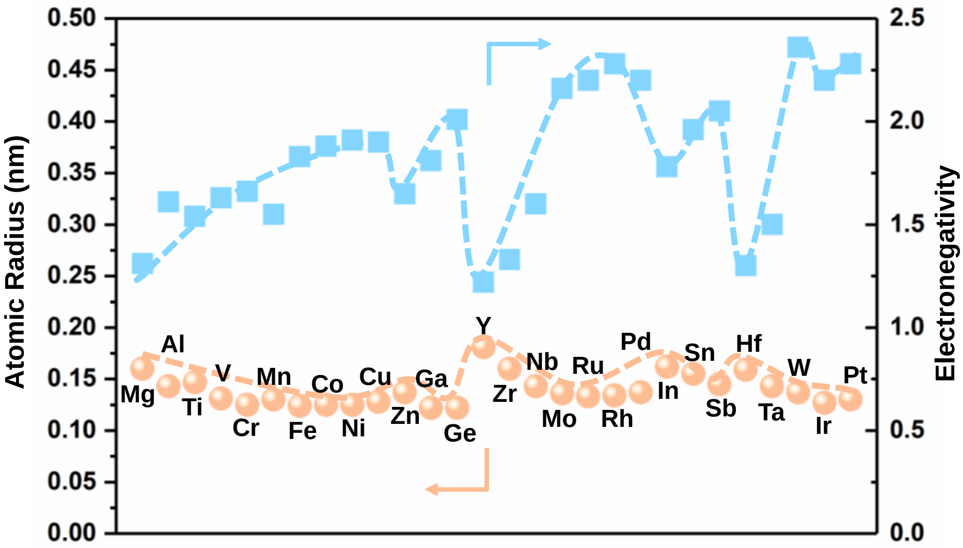

Supplementary Fig. 4 Atomic radius and electronegativity of multiple elements.

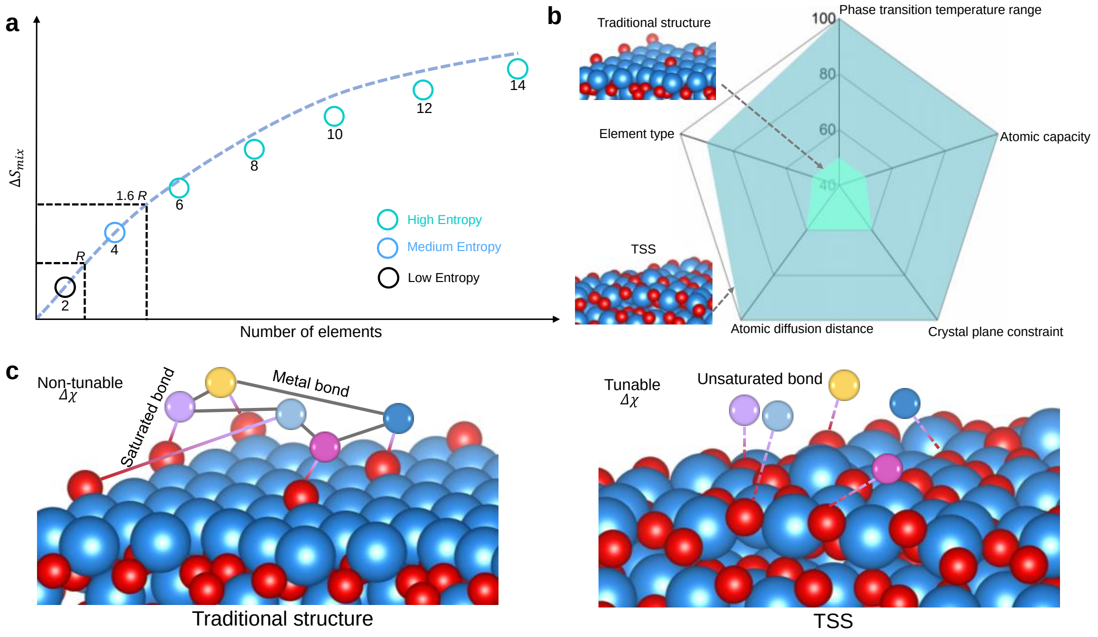

Supplementary Fig. 5 Thermodynamic modulation of electronegativity differences. a, Thermodynamic analysis mix entropy. **b**, Potential advantages of TSS. **c**, Unsaturated bonds formed between TSS and heteroatoms regulate their electronegativity difference.

Supplementary note 3

Nonclassical growth in HEAs:

The driving force for the growth of individual atom’s melt is

$$f = \frac{l\Delta T}{\Omega_S T_m}$$

Where l is the latent heat of melting of individual atom; ΔT is the supercooling; Ω_S is volume of individual atom; T_m represents melting point.

At low supersaturation, the free energy barrier is relatively large, any nucleated particles are unlikely to attachment other nearby particles, and the generation of critical nuclei is difficult, therefore, this process follows the classic growth pathway of monomers-by-monomers. At high supersaturation, the free energy barrier is relatively small and a greater number of particles are produced. When the supersaturation increases until the free energy barrier is equivalent to kT, the solution will undergo spinodal decomposition. At this time, a large number of particles will be produced, which increases the chance of contact growth of intermediates, especially when a metastable phase substrate is introduced into the system as confinement growth center, which promotes the stable progression of nonclassical growth pathway.

$$J = \beta Z C_0 \exp\left(-\frac{\Delta G^*}{kT}\right)$$

For metastable states, when infinitely deviating from them, the Gibbs free energy increases, and therefore the system immediately returns to its initial state. However, when the deviation is limited, the Gibbs free energy of the system may be smaller than the initial state, and the system cannot return to the initial state. On the contrary, it may transition to another metastable state. If Gibbs free energy is a continuous function, there must be a maximum value between two minima. This is the energy barrier that must be overcome to transition from a metastable state to a stable state. There is an energy barrier between metastable and stable states, which is a necessary condition for metastable states to exist without immediately transitioning to stable states. Therefore, introducing a metastable substrate into the system will promote the nonclassical growth pathway of adsorbates (Supplementary Fig. 6).

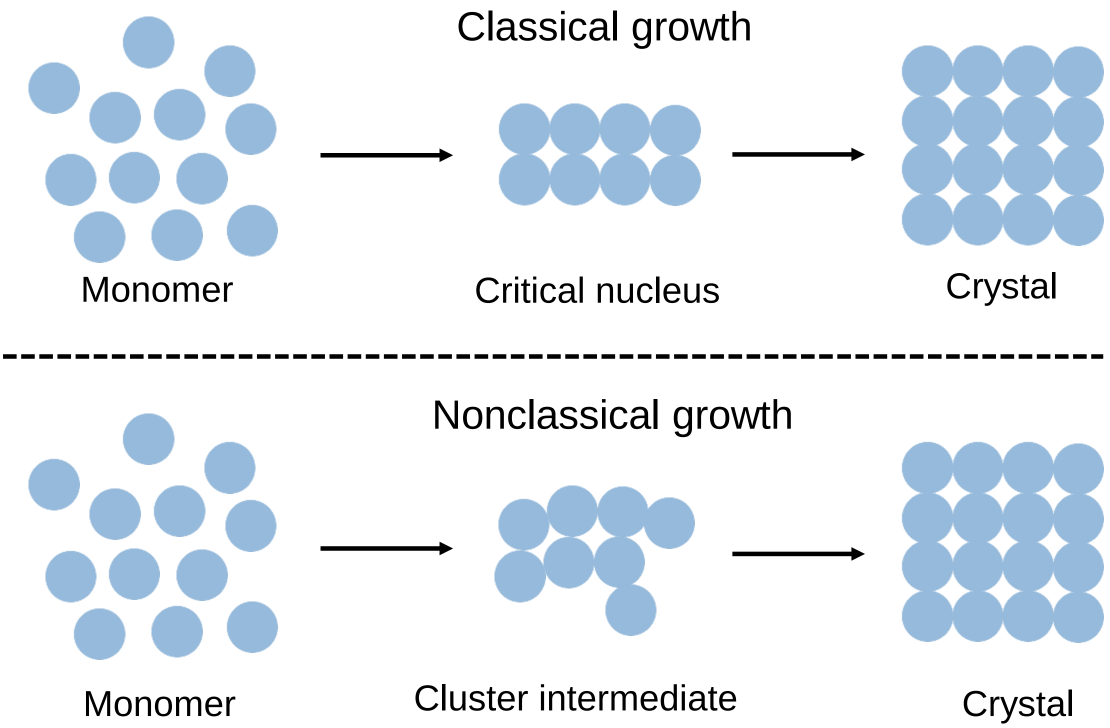

Supplementary Fig. 6 Pathways to crystallization by classical growth and nonclassical growth.

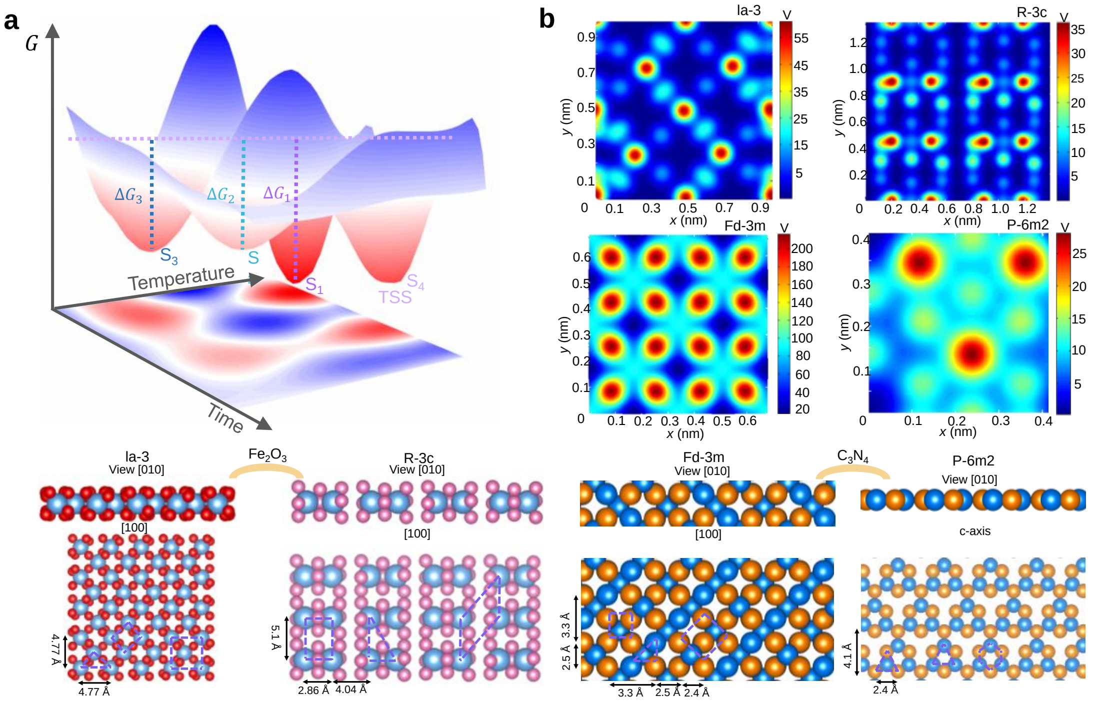

Supplementary Fig. 7 The thermodynamic state of TSS substrate. a, TSS modulated by Gibbs free energy. The S$_1$, S$_2$, S$_3$, and S$_4$, represent state 1, state 2, state 3 and TSS, respectively. **b,** Atomic mean potential and crystal structure of inorganic material Fe$_2$O$_3$ and organic material C$_3$N$_4$ with a periodic geometric structure.

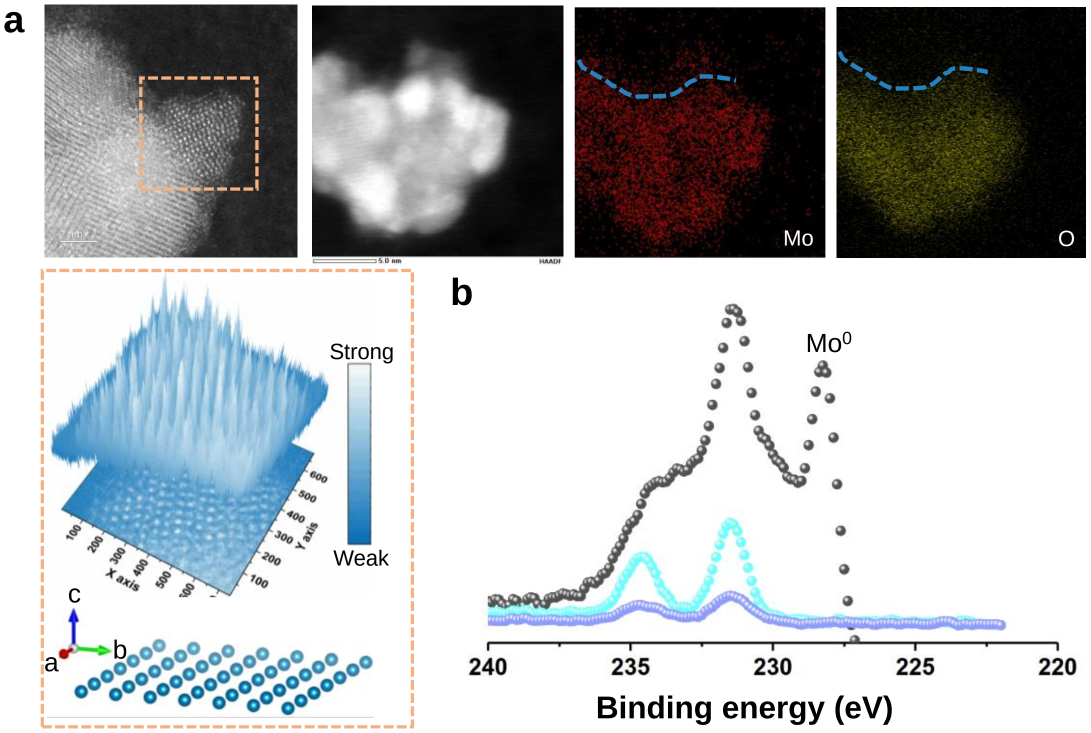

Supplementary Fig. 8 Mo Metallene formation through in-plane atomic attachment caused by TSS surface supersaturation. a, HAADF-STEM images and STEM elemental mappings of Mo metallene/β-Fe_2O_3. 3D intensity surface plot and crystal structure of Mo metallene. **b**, Mo 3*d* x-ray photoelectron spectroscopy of Mo metallene. A very obvious metallic bond was detected.

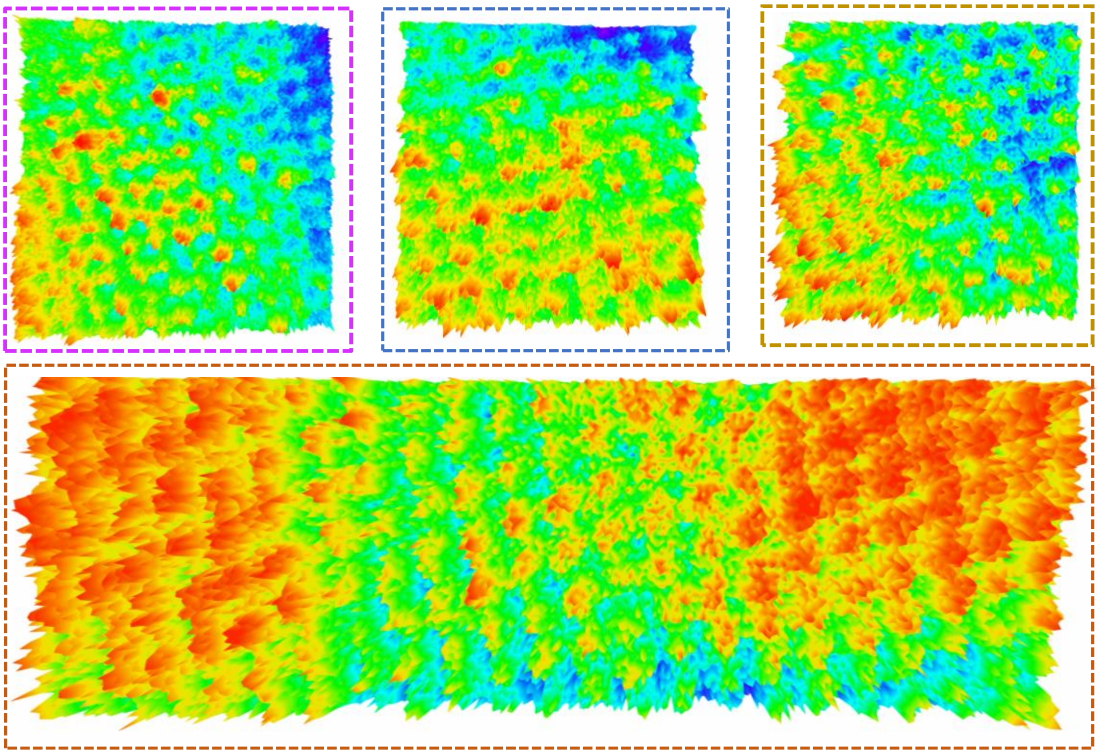

Supplementary Fig. 9 Structural characterization of HESA. 3D intensity surface images shown for the dashed regions of the image in Fig. 2**a**.

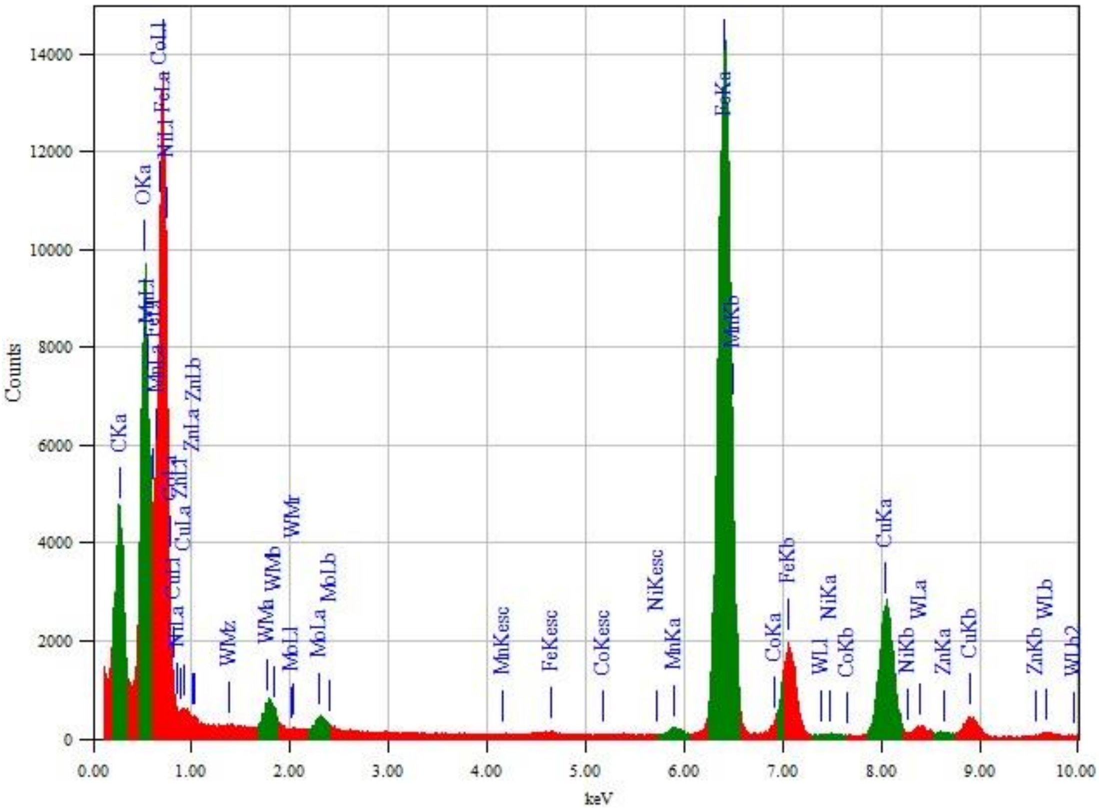

Supplementary Fig. 10 STEM-EDX spectrum of the HESA.

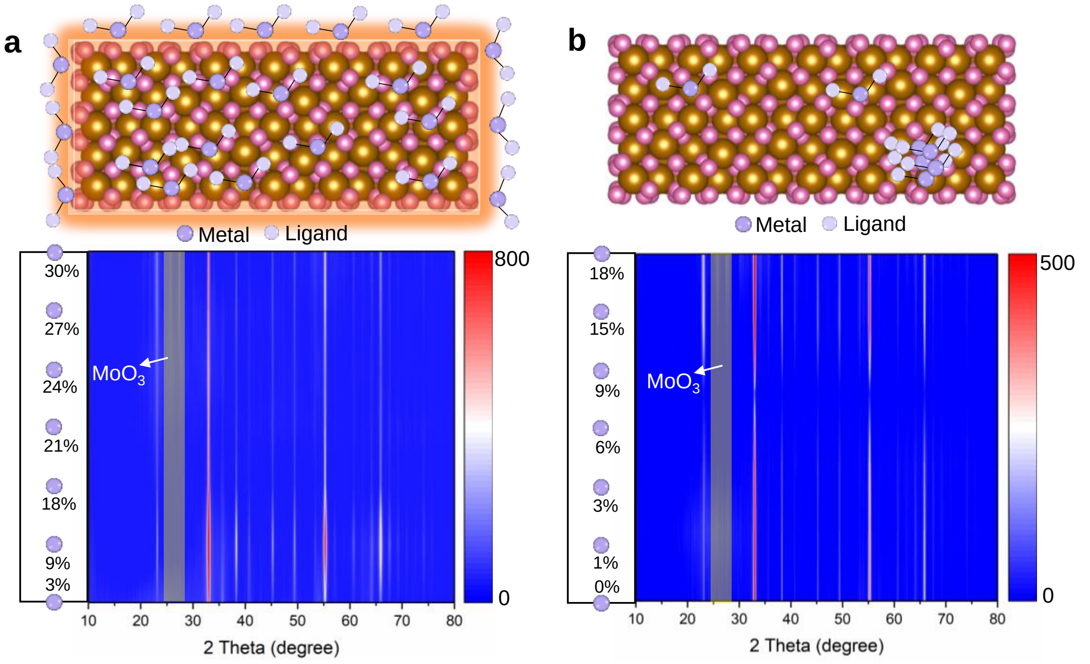

Supplementary Fig. 11 XRD patterns of samples following nonclassical growth pathway and classical growth pathway, respectively. a, Nonclassical growth pathway: XRD patterns of samples with different Mo contents constructed on β-Fe_2O_3 TSS. **b**, Classical growth pathway: XRD patterns of samples with different Mo contents constructed on holocrystalline β-Fe_2O_3.

We compared the TSS and holocrystalline β-Fe_2O_3 as substrate for Mo precursors loading, respectively. As shown in Supplementary Fig. 11, the Mo content on the TSS substrate surface exceeded 20% without the formation of MoO_3. In contrast, significant MoO_3 was detected on the holocrystalline β-Fe_2O_3 when the Mo content surpassed 9%, highlighting the supersaturation characteristics unique to the TSS surface.

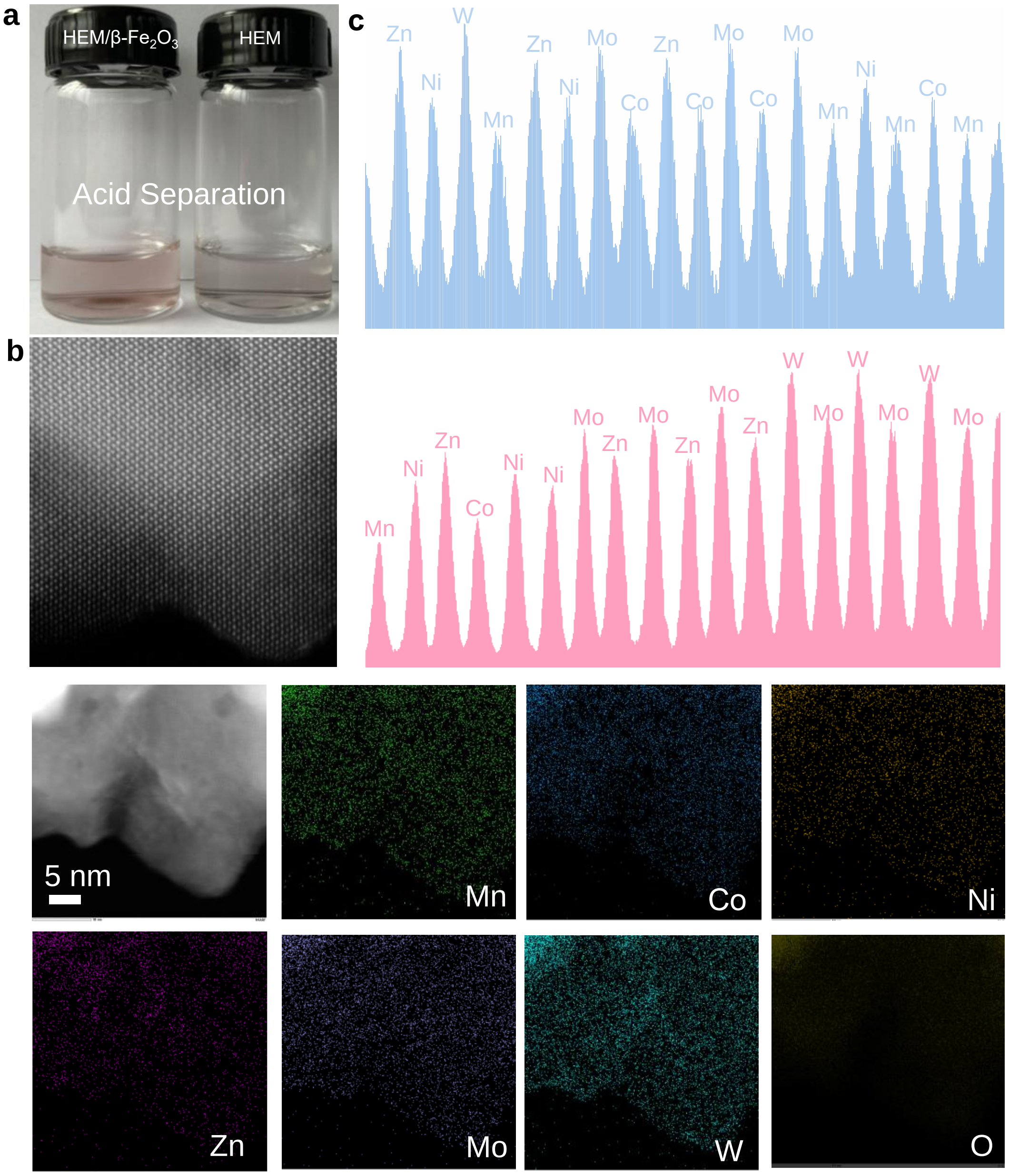

Supplementary Fig. 12 Structural characterization of HEM. a, The optical photo of solutions separated with dilute hydrochloric acid. **b**, HAADF-STEM image and STEM elemental mappings of HEM. **c**, Intensity surface plot along the line in Fig. 2**a** measured along the projection of the *c* axis.

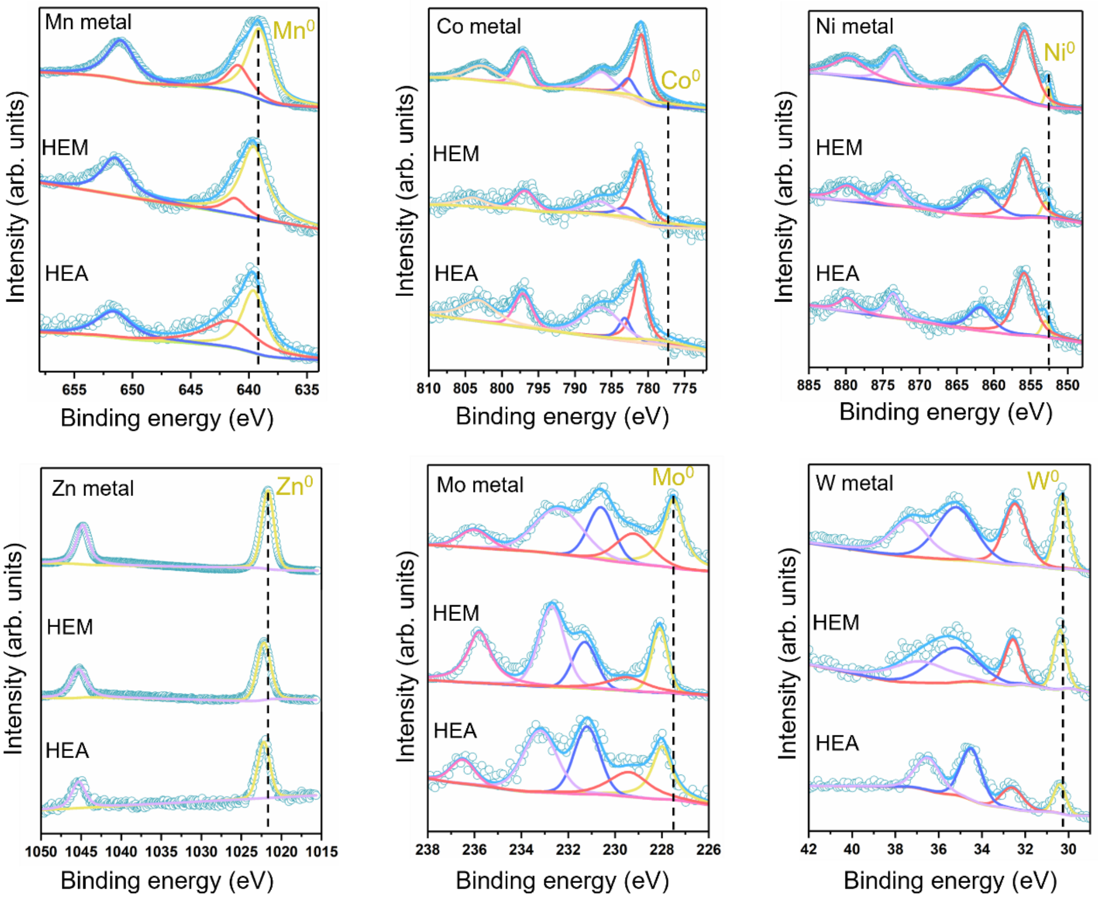

Supplementary Fig. 13 High resolutions XPS analysis of Mn 3*s*, Mn 2*p*, Co 2*p*, Ni 2*p*, Zn 2*p*, Mo 3*d* and W 4*f* of freshly synthesized HEM and bulk HEA samples. The reference bulk HEA sample was obtained by melting a mixture of pure metals at 3973K using non-consumable vacuum arc melting technology.

We utilized the high resolutions XPS to investigate the surface chemical states of fresh pure metals, HEA, and HEM. The full XPS spectrum confirms the coexistence of Mn, Co, Ni, Zn, Mo, and W elements in the synthesized HEA and HEM samples. Additionally, it reveals that due to the enhanced oxygen state on the sample surface, Mn^0, Co^0, Ni^0, Zn^0, Mo^0, and W^0 partially transition into their corresponding ion peaks (Supplementary Fig. 13). The shift of the zero-valent metal peak toward higher binding energy suggests the formation of metal alloys. This phenomenon arises because, during XPS analysis of metals, X-rays irradiate the sample surface, photoionizing the inner electrons of atoms and generating photoelectrons. Alongside the main photoelectron peaks, companion peaks, including ion peaks, may also appear. For metallic samples, XPS typically probes a depth of 0.5 to 2 nm, where slight oxidation of surface atoms can lead to the detection of ion peaks (Supplementary Fig. 14). Such observations are common in pure metals and high-entropy alloy materials.

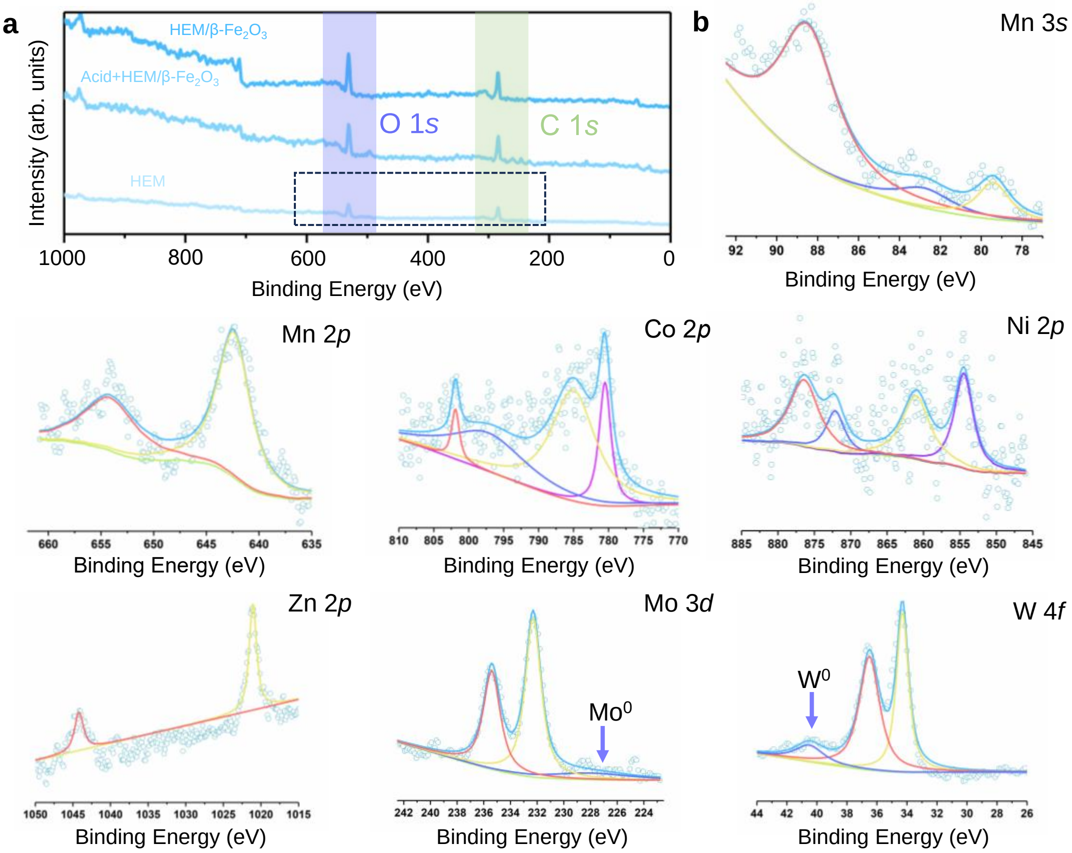

Supplementary Fig. 14 XPS analysis of HEM following an extended storage period. **a**, XPS survey spectra of different samples. In the XPS survey spectra of HEM and HEM/β-Fe_2O_3, the characteristic O peaks become negligible after the acid separation, implying purified HEM were obtained. **b**, High resolutions of Mn 3*s*, Mn 2*p*, Co 2*p*, Ni 2*p*, Zn 2*p*, Mo 3*d* and W 4*f*. Despite inevitable oxidation of the edges in the air, peaks of Mo^0 and W^0 were still detected.

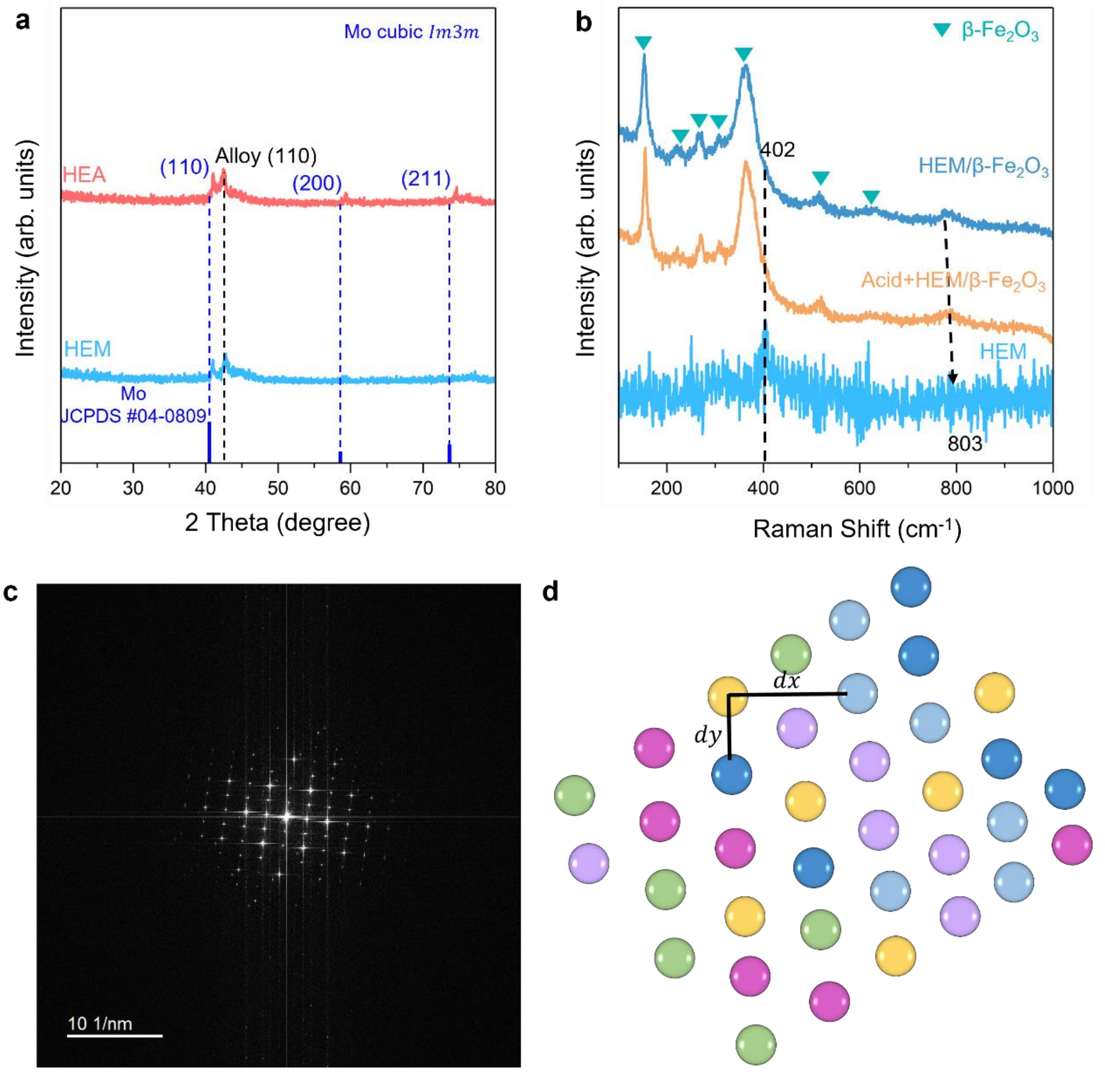

Supplementary Fig. 15 Structural analysis of HEM. a, XRD patterns. **b,** Raman spectra. **c**, The FFT pattern of HEM. **d**, Schematic diagram of HEM structure drawn based on atomic distribution information. d_x and d_y represent the atomic spacings in the x and y directions, which are used to calculate atomic discrete distribution.

The powder XRD patterns (Supplementary Fig. 15a) indicate that both the HEM and HEA exhibit a single-phase body-centered cubic structure with distinct diffraction peaks attributed to (110), (200), and (211) planes, which aligns closely with the standard PDF cards for Mo, characterized by the cubic space group $Im3m$. Further Raman analysis reveals vibrational peaks at ~402 $\mathrm{cm^{-1}}$, characteristic of the Mo metallic phase, along with its second overtone observed at ~803 $\mathrm{cm^{-1}}$. The atomic-resolution HAADF-STEM image and the FFT pattern (Supplementary Fig. 15c) demonstrate the high-quality crystallinity of HEM.

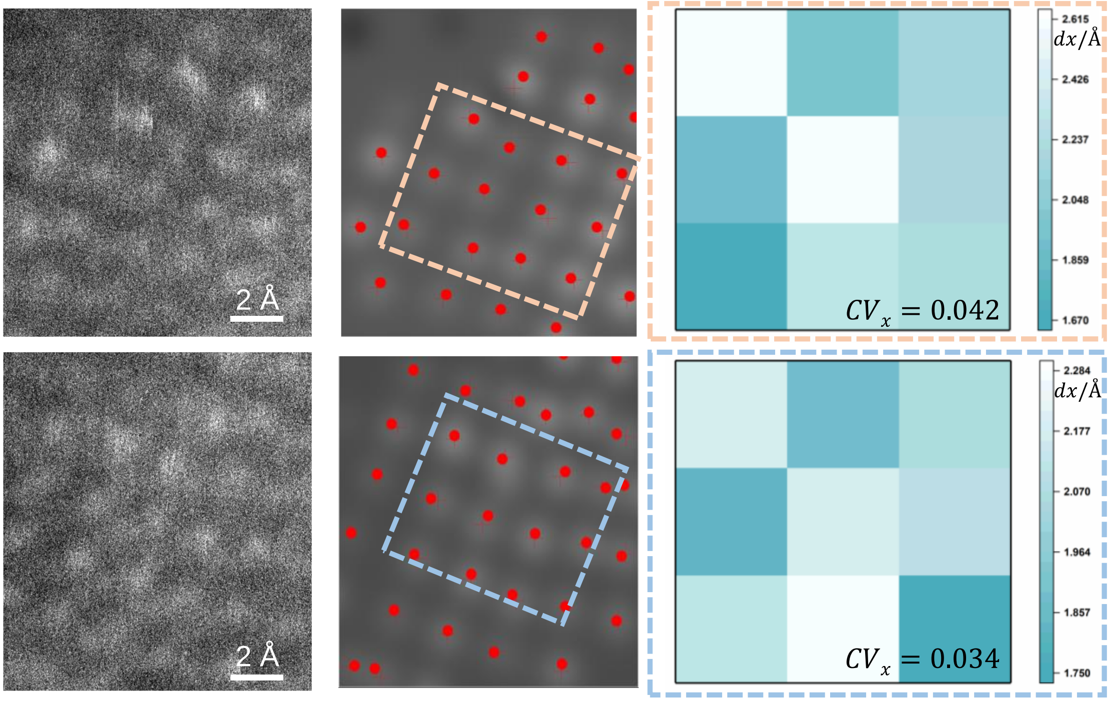

Supplementary Fig. 16 Atomic simulations and atomic discrete distribution maps for different regions of $Mo_1/\beta\text{-}Fe_2O_3$ in Fig. 2a (a1).

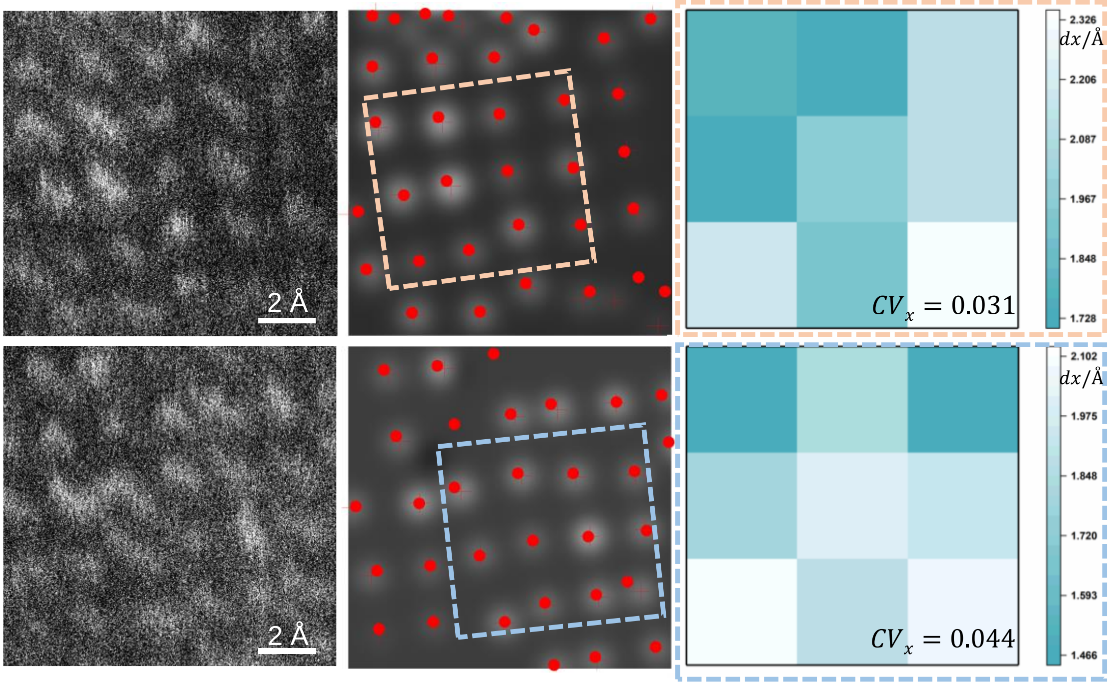

Supplementary Fig. 17 Atomic simulations and atomic discrete distribution maps for different regions of $(MoW)_1/\beta\text{-}Fe_2O_3$ in Fig. 2a (a2).

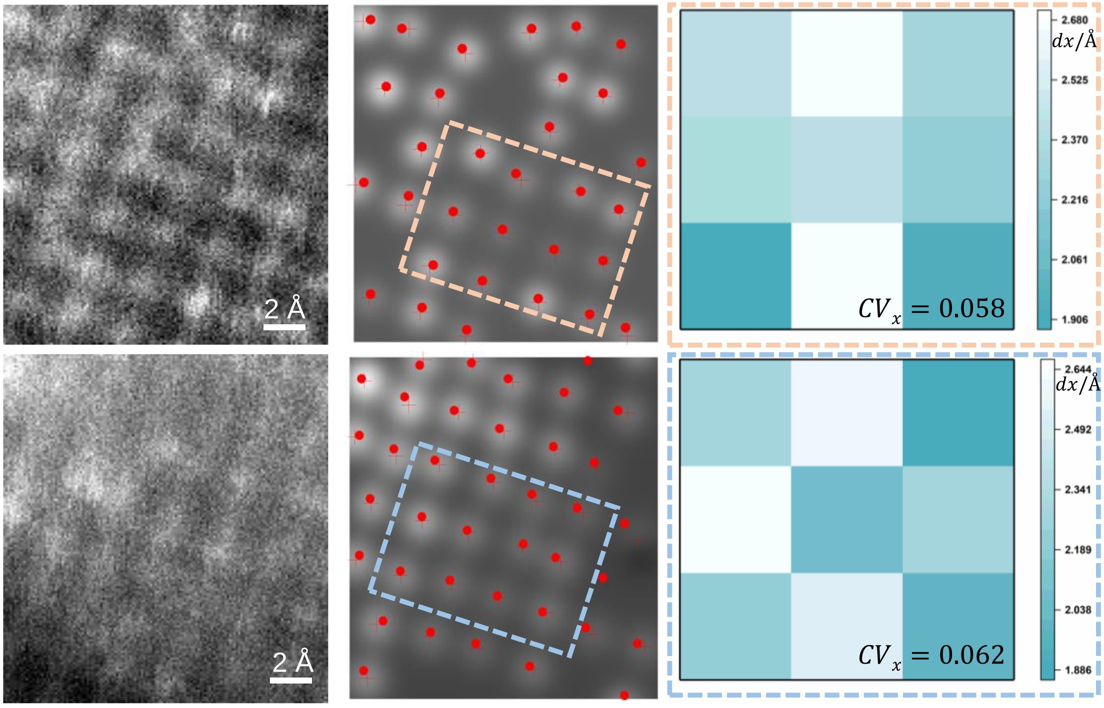

Supplementary Fig. 18 Atomic simulations and atomic discrete distribution maps for different regions of $(MnMoW)_1/\beta\text{-}Fe_2O_3$ in Fig. 2a (a3).

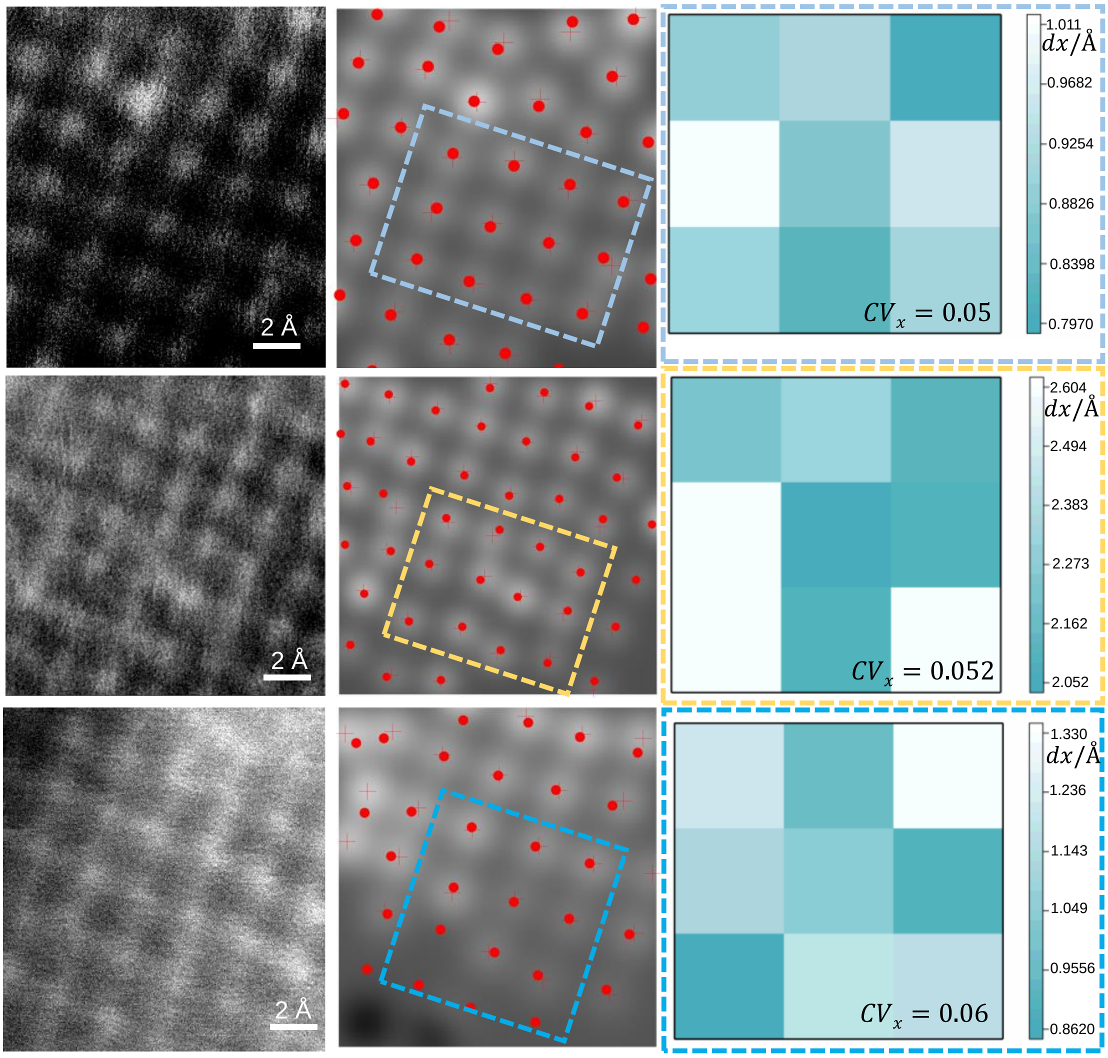

Supplementary Fig. 19 Atomic simulations and atomic discrete distribution maps for different regions of HESA in Fig. 2a (a4).

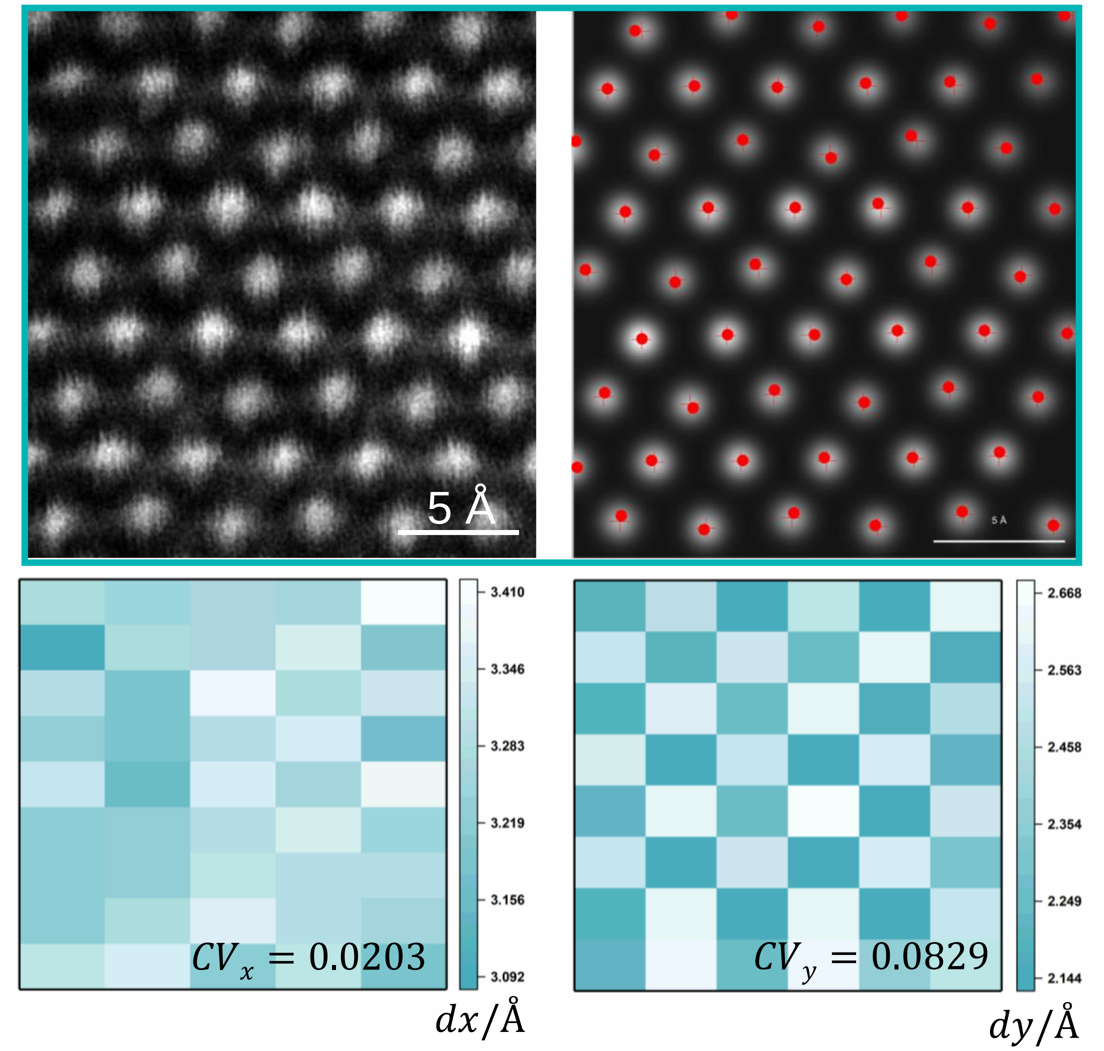

Supplementary Fig. 20 Atomic simulations and atomic discrete distribution maps for different regions of HEM in Fig. 2a (a5).

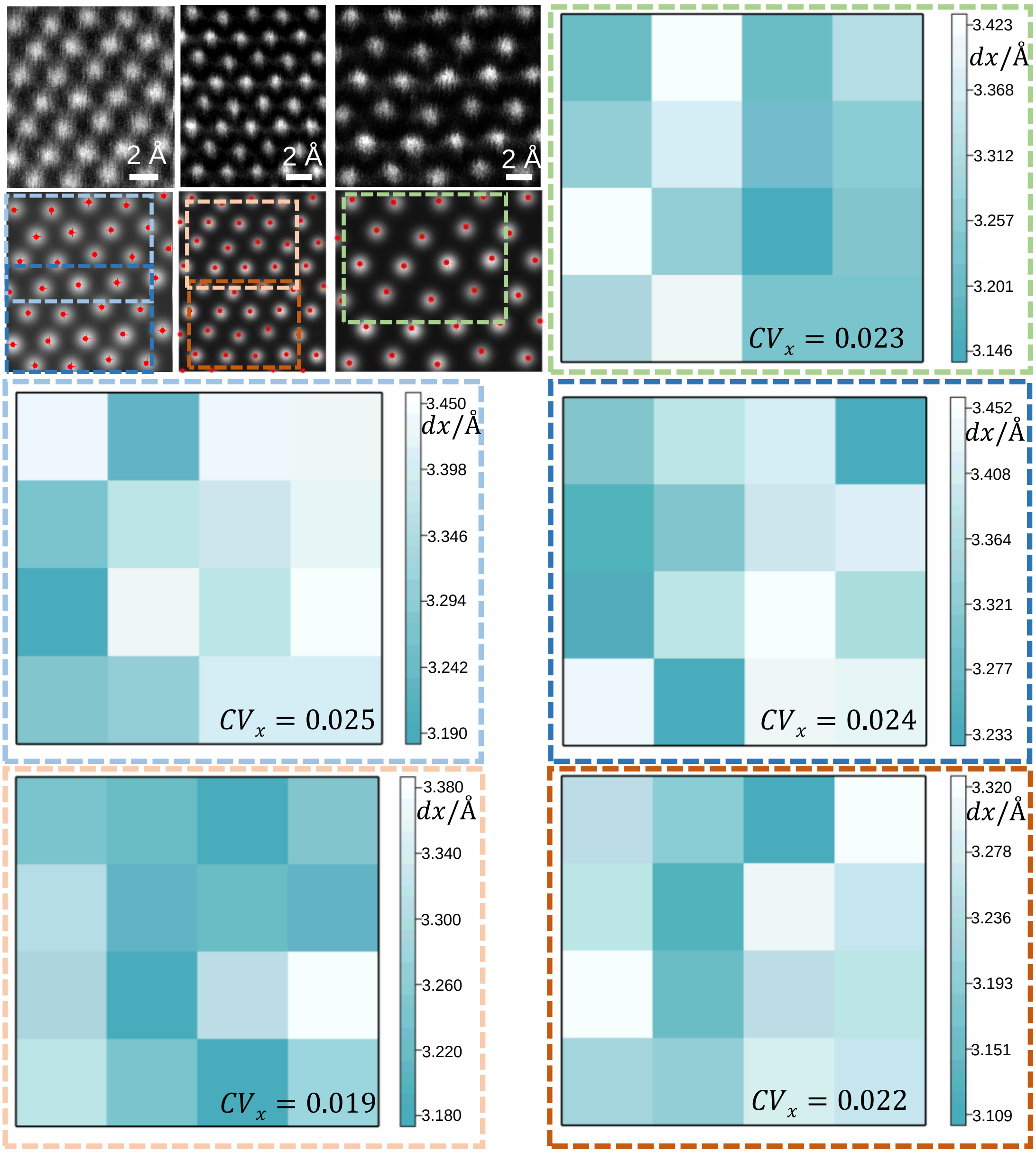

Supplementary Fig. 21 Atomic simulations and atomic discrete distribution maps for different regions of HEM in **Fig. 2a** (a5).

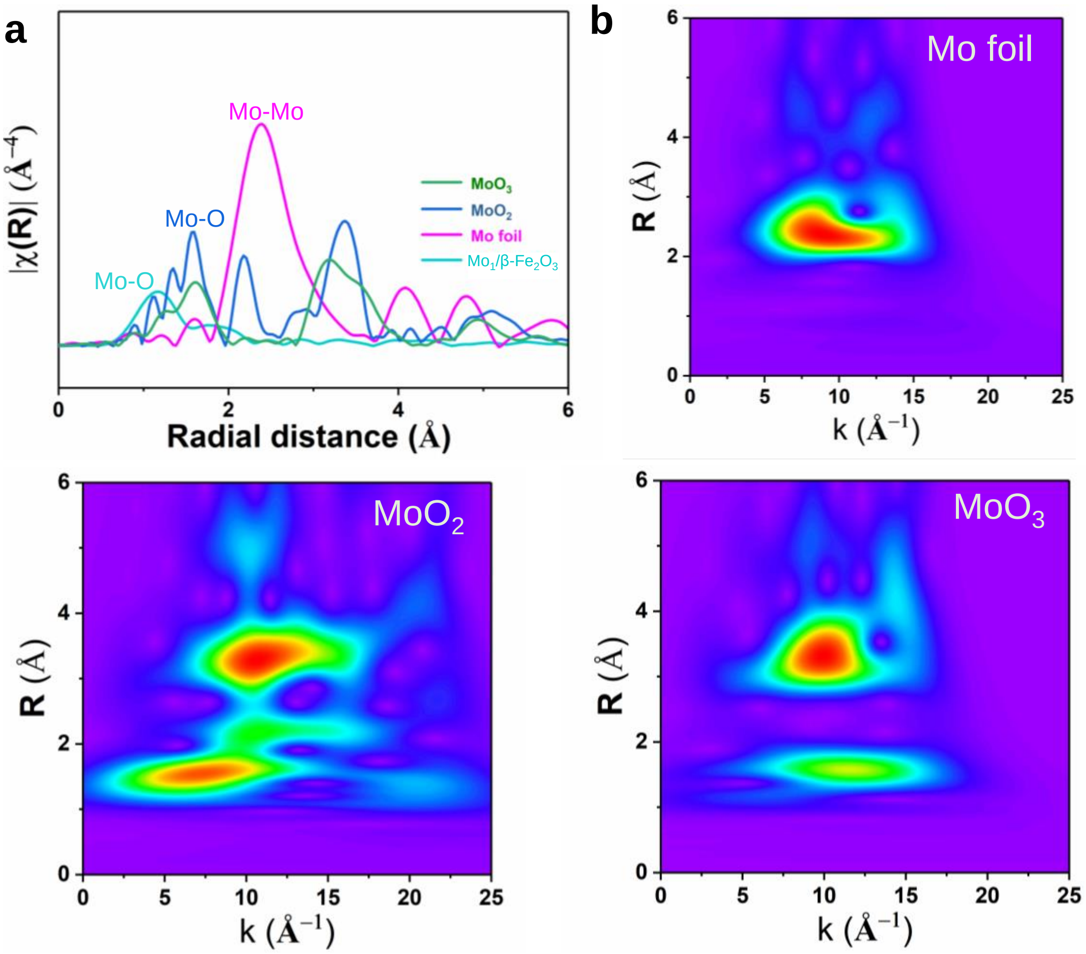

Supplementary Fig. 22 EXAFS analysis. **a**, Mo K-edge Fourier-transformed EXAFS result for $Mo_1/\beta\text{-}Fe_2O_3$. **b**, Wavelet-transformed EXAFS of reference samples.

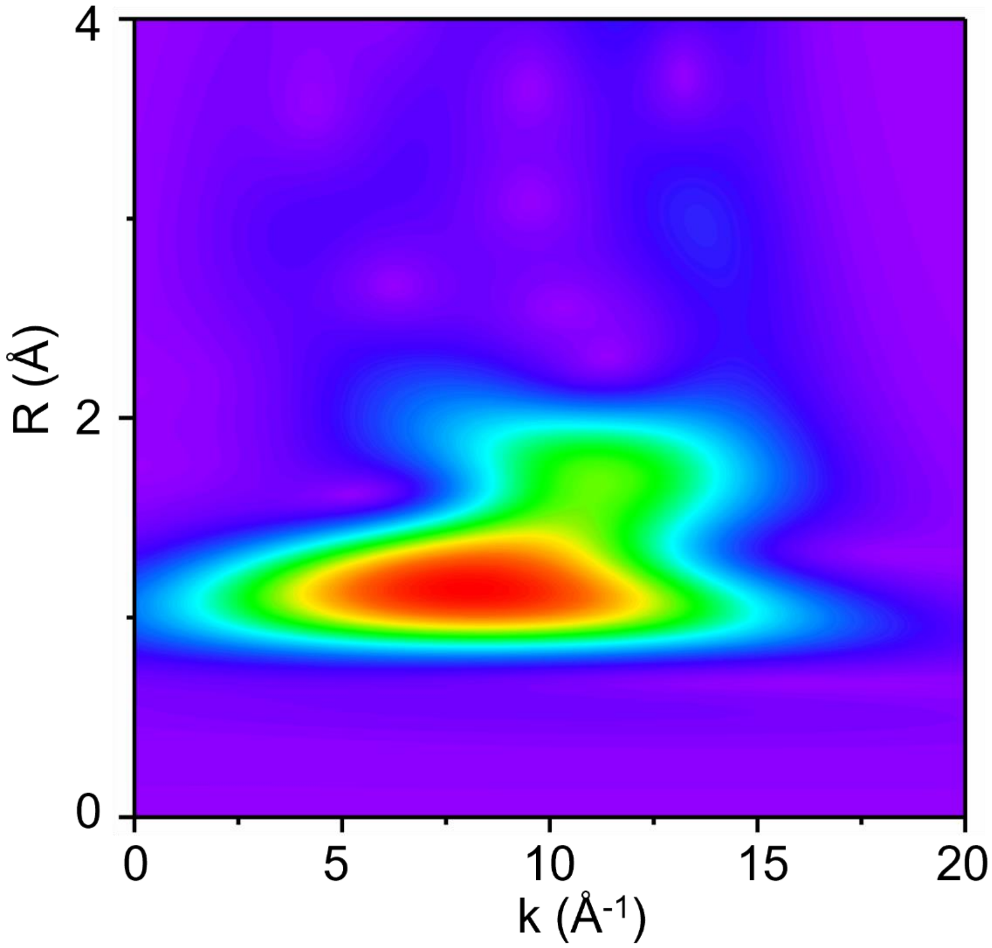

Supplementary Fig. 23 Wavelet-transformed EXAFS of $Mo_1/\beta\text{-}Fe_2O_3$.

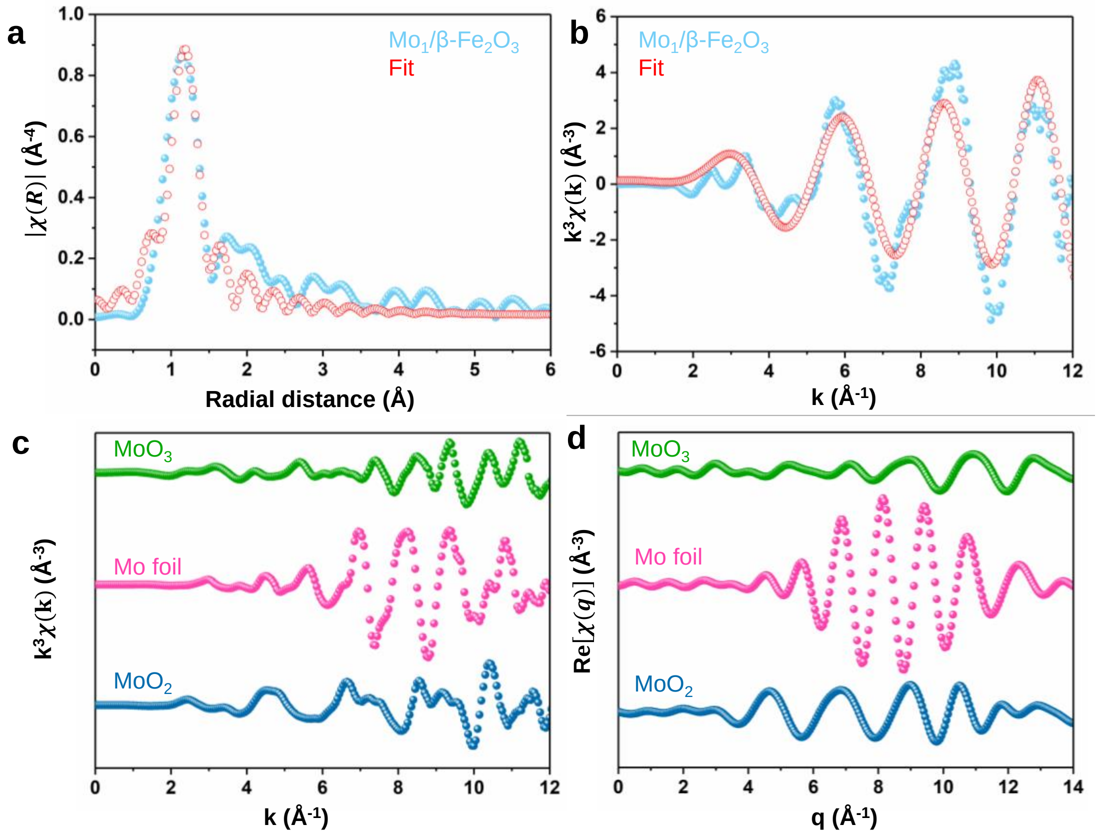

Supplementary Fig. 24 Mo K-edge EXAFS fitting results of Mo_1/β-Fe_2O_3. a, *R*-space. **b**, *k*-space. **c**, *k*-space of the reference samples. **d**, *q*-space of the reference samples.

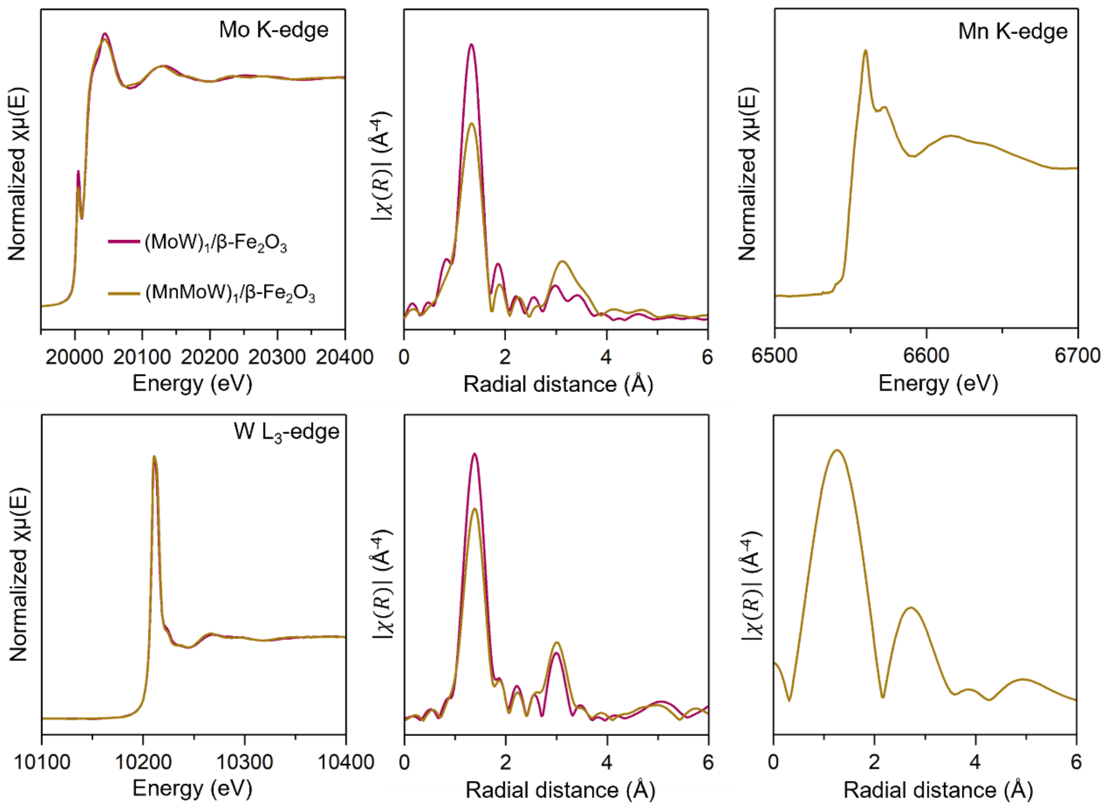

Supplementary Fig. 25 XANES and Fourier transformed EXAFS spectra of (MoW)$_1$/β-Fe$_2$O$_3$ and (MnMoW)$_1$/β-Fe$_2$O$_3$. Mn K-edge; Mo K-edge; W L$_3$-edge.

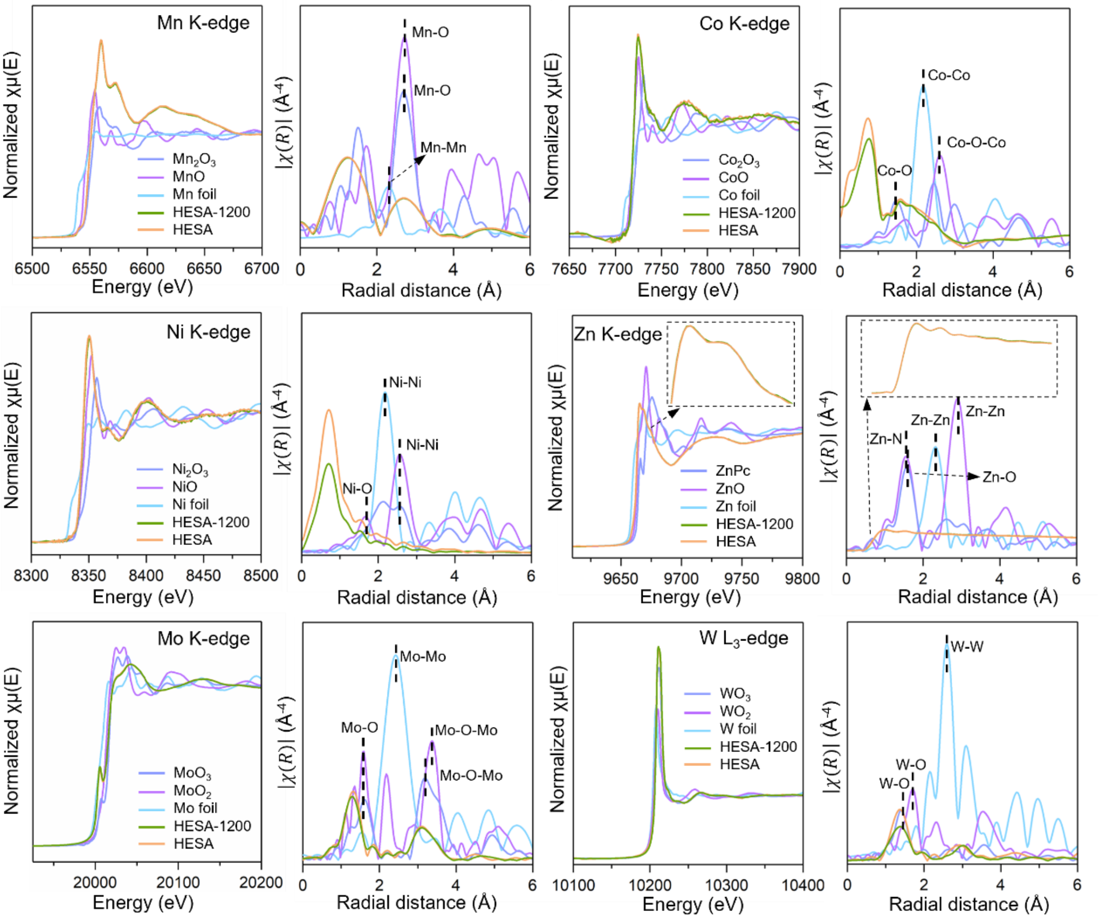

Supplementary Fig. 26 XANES spectra and Fourier-transformed EXAFS spectra of the HESA sample. The XANES results reveal the intrinsic properties of the unsaturated valence states in all elements. The Fourier-transformed EXAFS spectra show a distinct M-O first coordination shell with no evidence of metal-metal coordination.

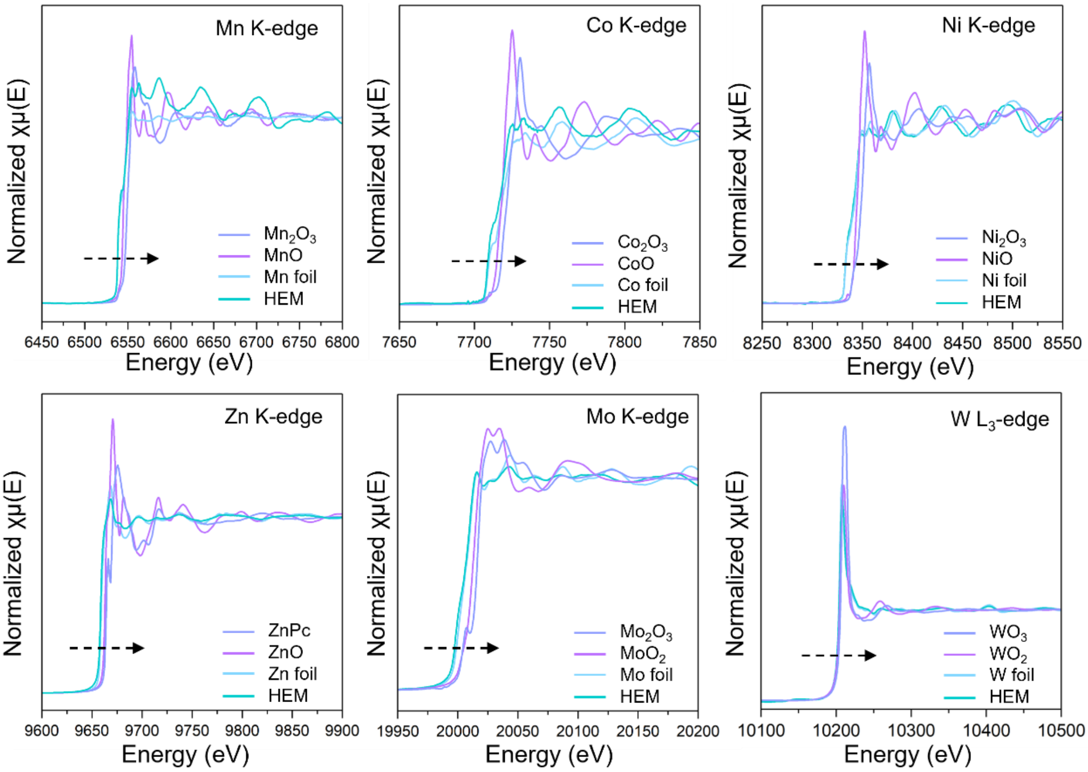

Supplementary Fig. 27 XANES spectra of the HEM and reference samples.

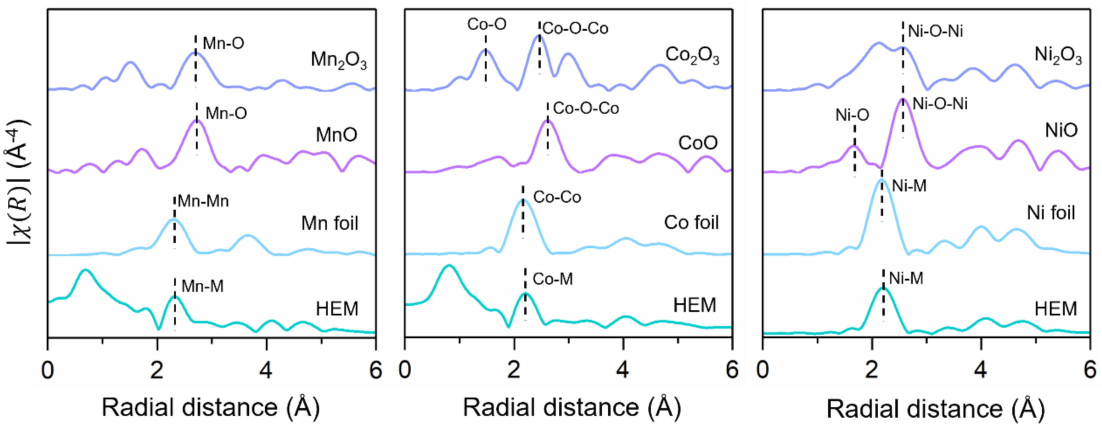

Supplementary Fig. 28 Fourier-transformed EXAFS spectra of the HEM sample. Mn K-edge; Co K-edge; Ni K-edge.

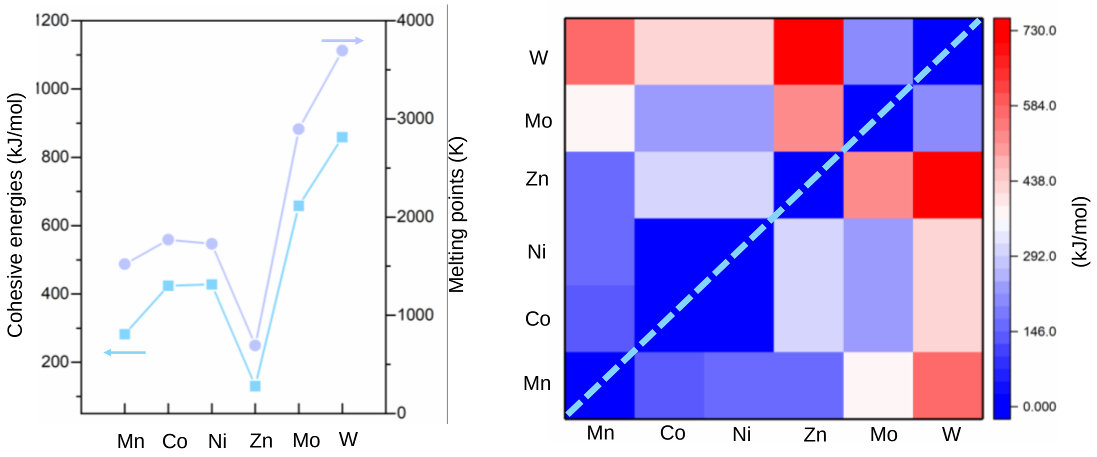

Supplementary Fig. 29 Cohesion energy and distribution of metal melting points of Mn, Co, Ni, Zn, Mo, and W.

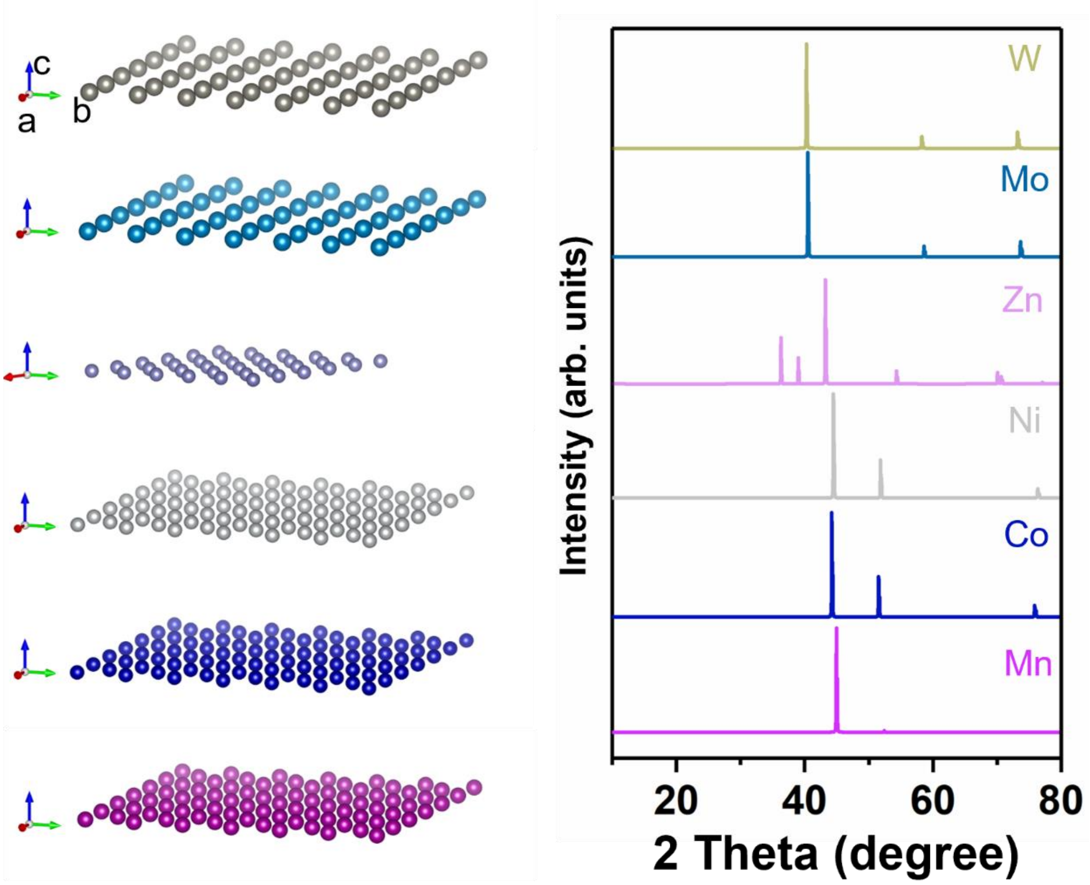

Supplementary Fig. 30 Structural characteristics of various metals. Crystallographic structure of metal and fitted XRD patterns.

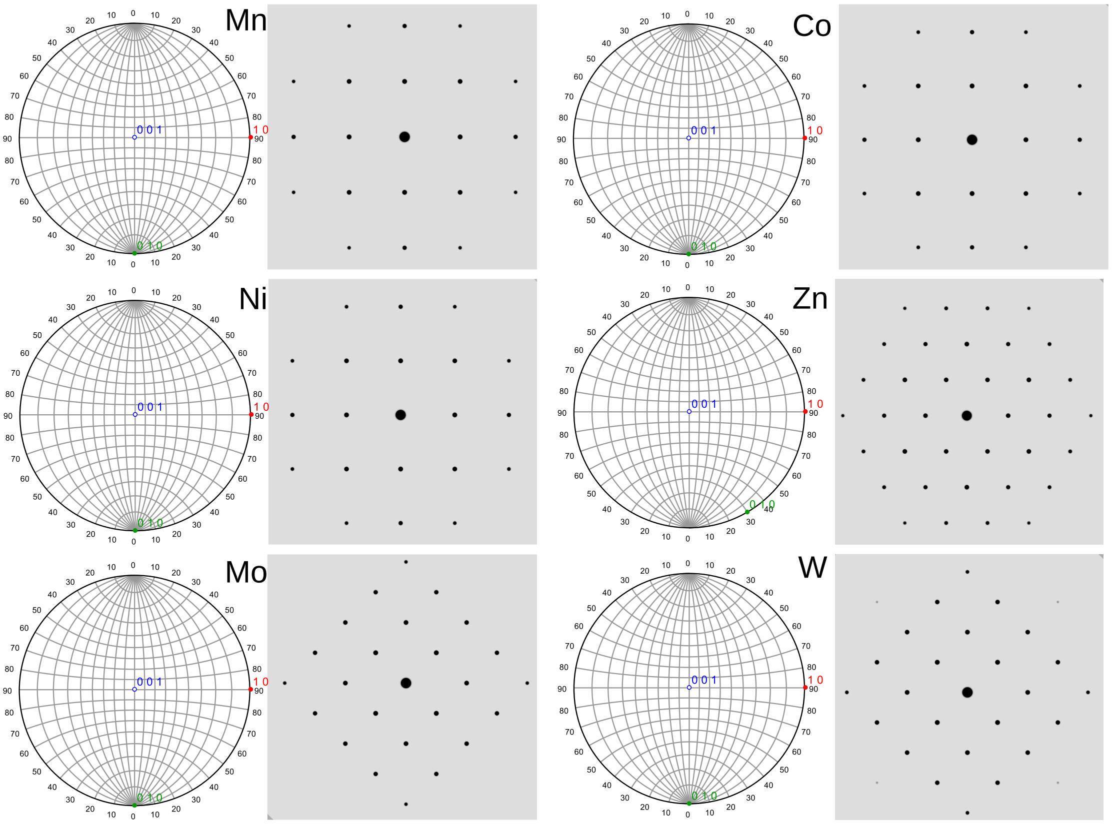

Supplementary Fig. 31 Simulated electron diffraction pattern oriented along the [001] direction. Mn, Co and Ni maintain highly similar pattern, while Mo and W maintain highly similar pattern.

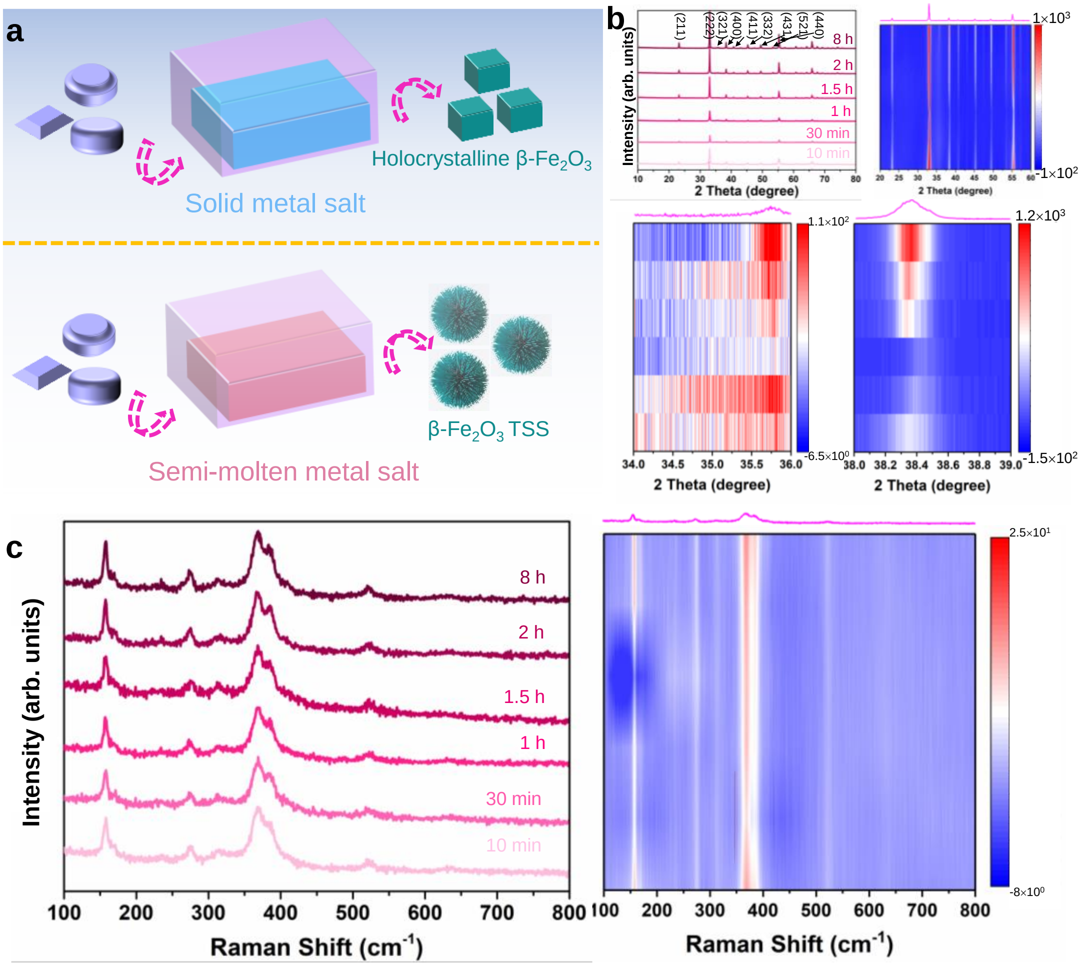

Supplementary Fig. 32 XRD and Raman studies of holocrystalline β-Fe_2O_3 and β-Fe_2O_3 TSS substrate. **a**, Schematic diagram of the alkali metal salts-assisted synthesis process. **b**, XRD patterns of β-Fe_2O_3 under different semi-molten metal salt treatment times and enlargement of XRD patterns. 10 min and 8 h: holocrystalline β-Fe_2O_3; 30 min, 1 h, 1.5 h and 2 h: β-Fe_2O_3 TSS. **c**, Raman spectra of β-Fe_2O_3 under different semi-molten metal salt treatment times.

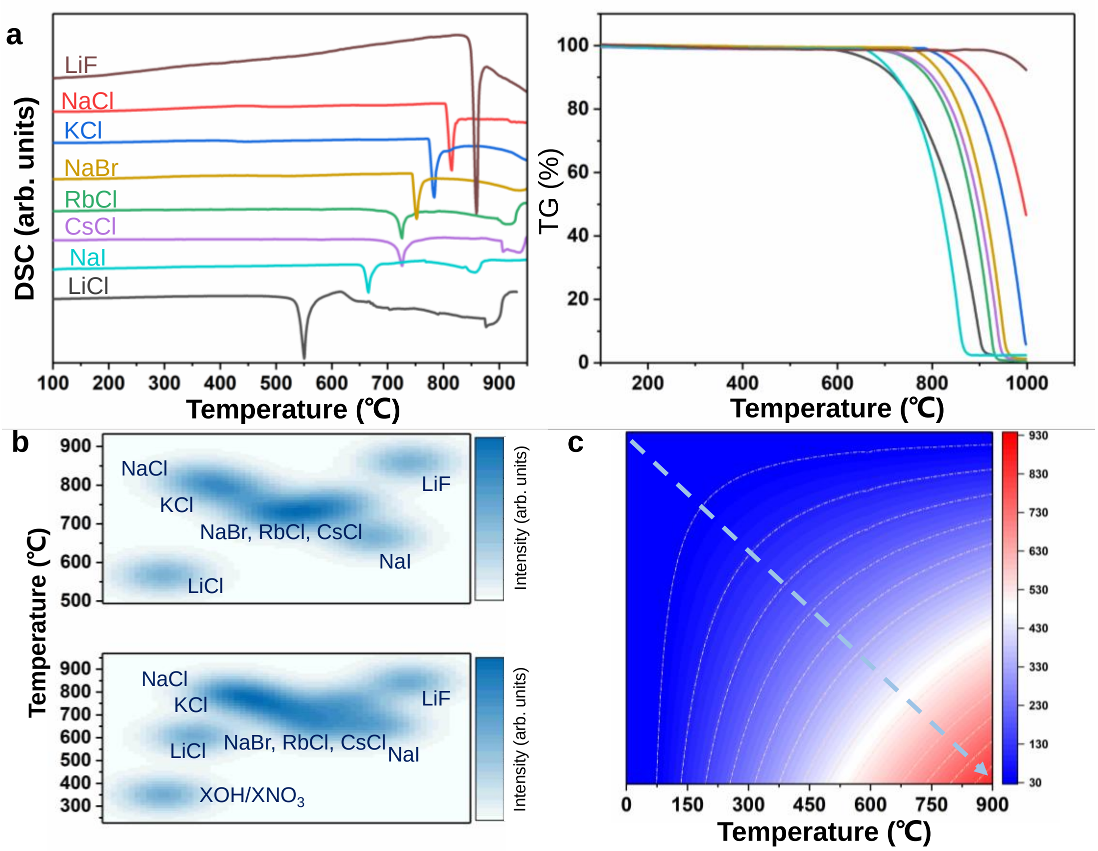

Supplementary Fig. 33 TG-DSC curves of alkali metal salts. a, DSC curves and TG curves. **b**, Experimental melting temperature and theoretical melting temperature of metal salts obtained from TG-DSC results. **c**, Thermal temperature field distribution of alkali molten salt fitted based on TG-DSC curves.

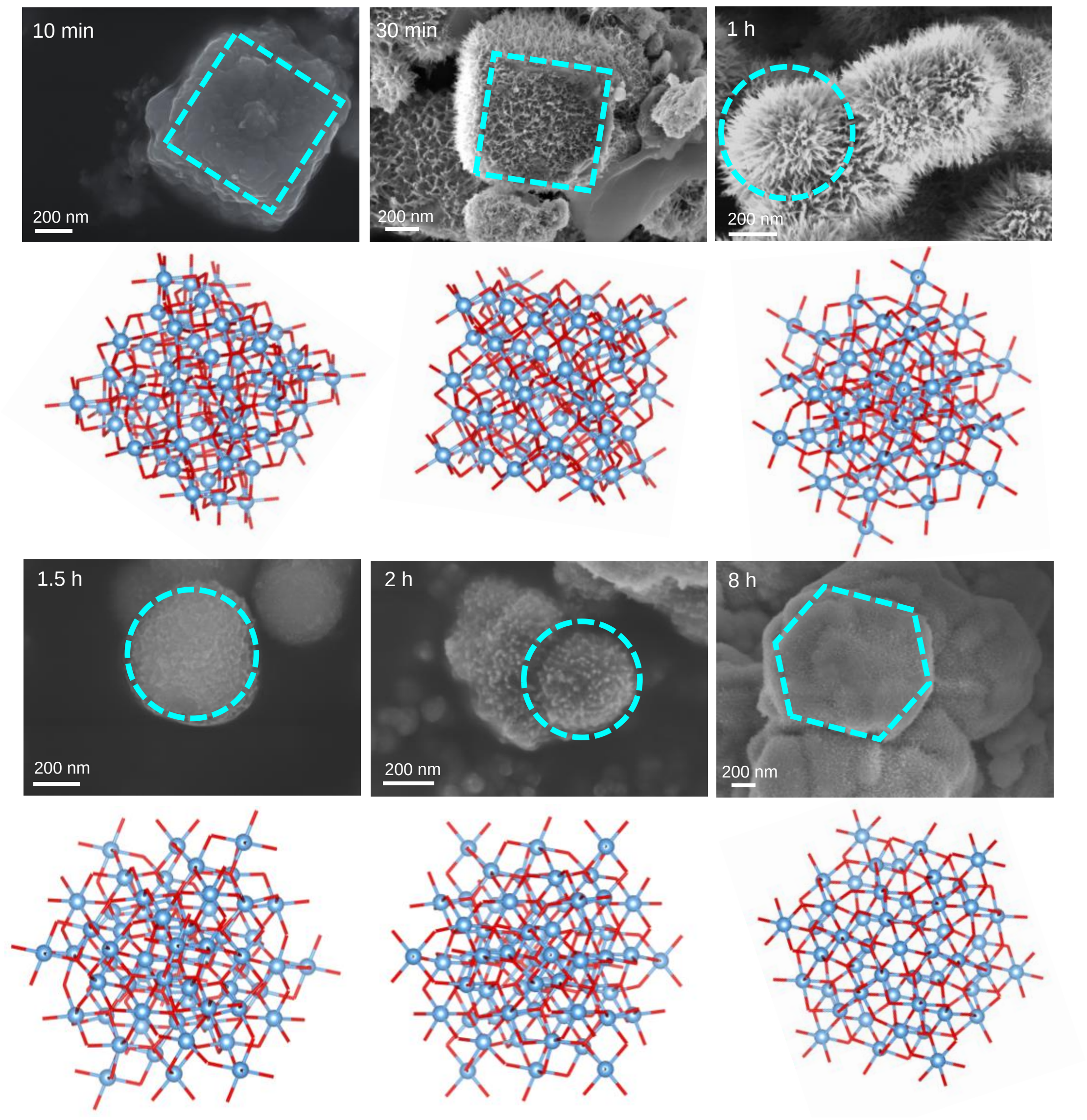

Supplementary Fig. 34 SEM images analysis of β-Fe_2O_3 TSS evolution over time. Light blue balls represent Fe atoms.

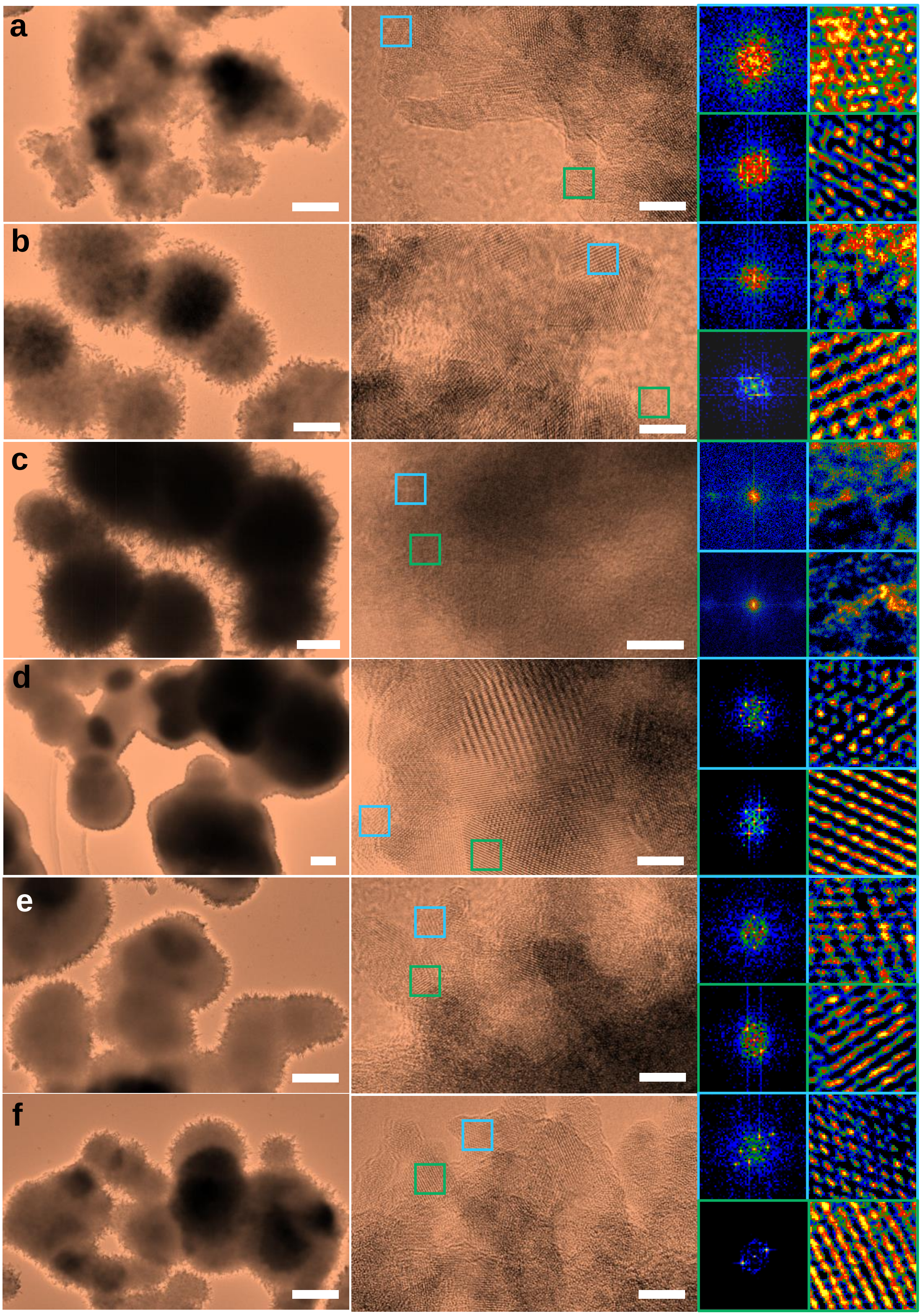

Supplementary Fig. 35 TEM analysis of the β-Fe_2O_3 TSS. a, TEM image, HRTEM image, the selected areas fast Fourier transform patterns and inverse fast Fourier transform patterns of β-Fe_2O_3 after 10 minutes, 30 min (**b**), 1 h (**c**), 1.5 h (**d**), 2 h (**e**) and 8h (**f**) of metal salts-assisted treatment. Scale bar, 200 nm.

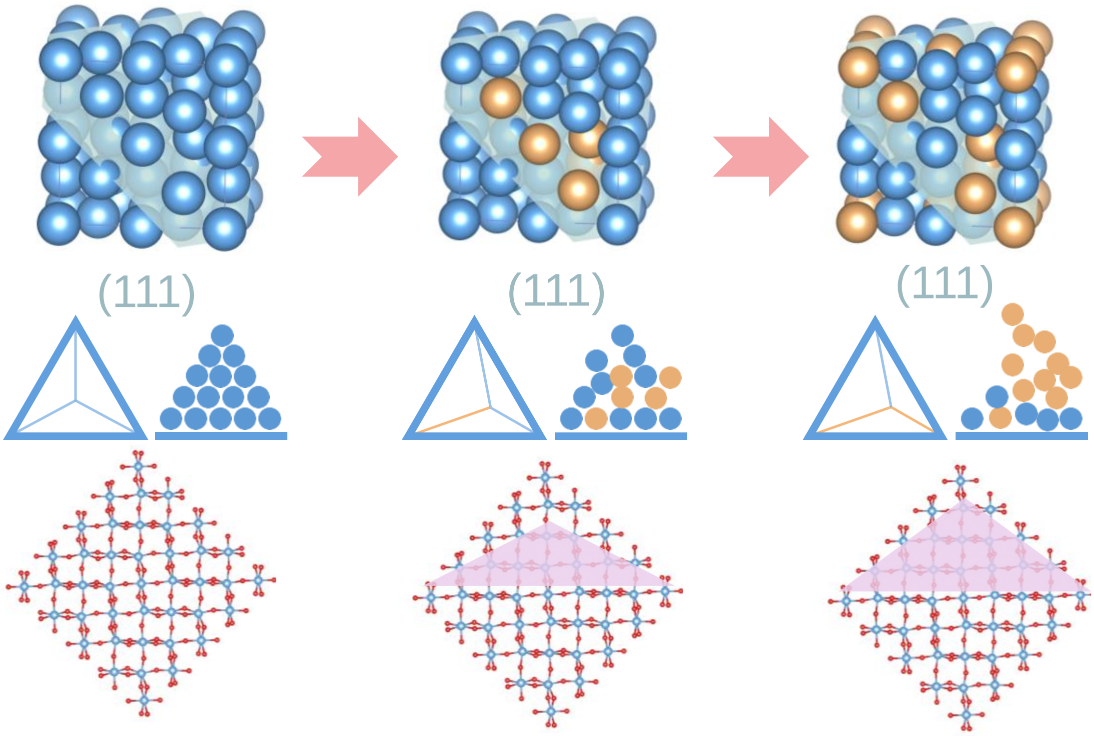

Supplementary Fig. 36 Schematic diagram of β-Fe_2O_3 TSS formation along the [111]. Light blue and red balls represent iron atoms and oxygen atoms, respectively. The yellow ball represents the appearance of disordered iron atoms.

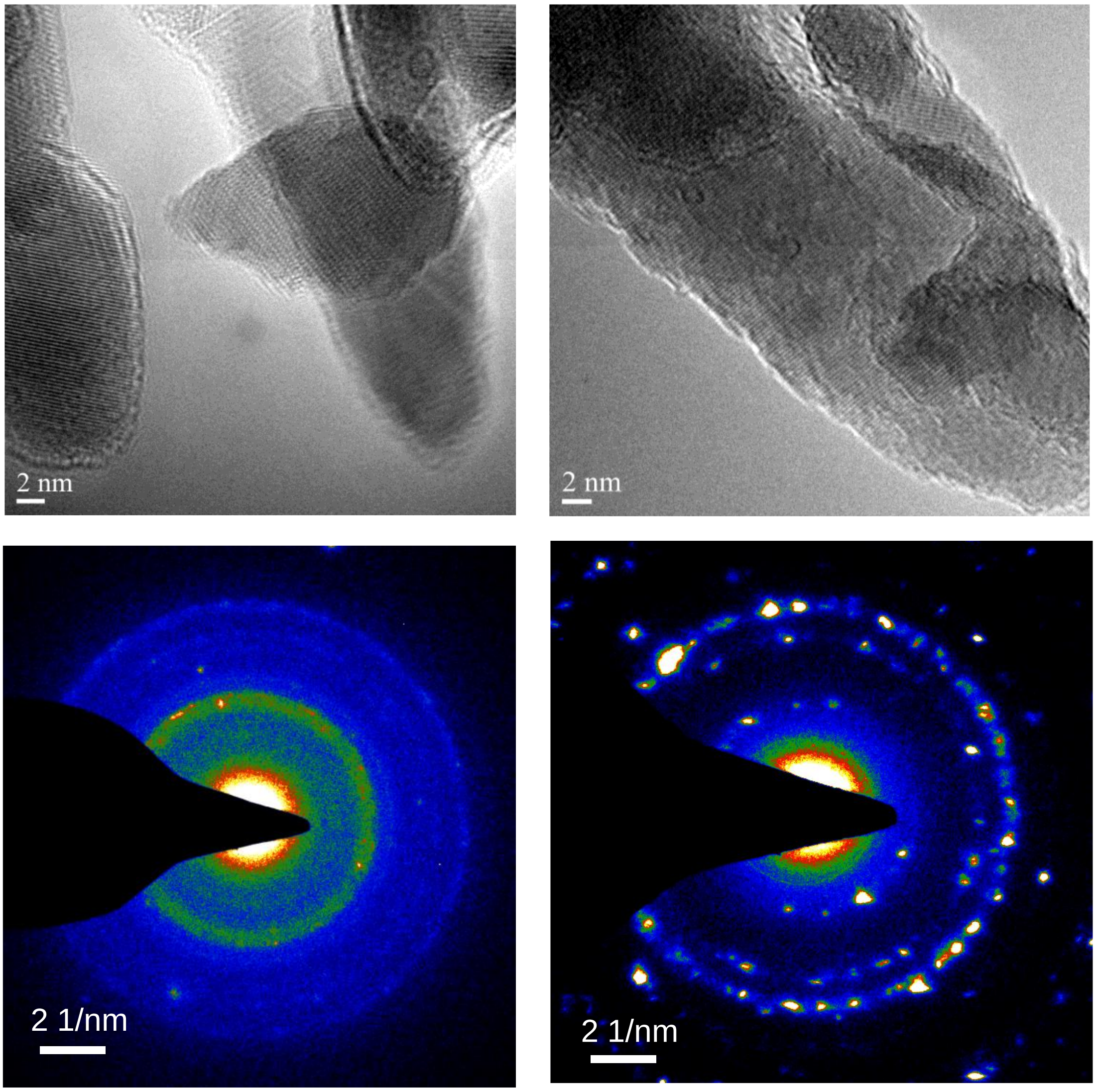

Supplementary Fig. 37 SAED patterns of β-Fe_2O_3 TSS before and after high energy electron beam irradiation.

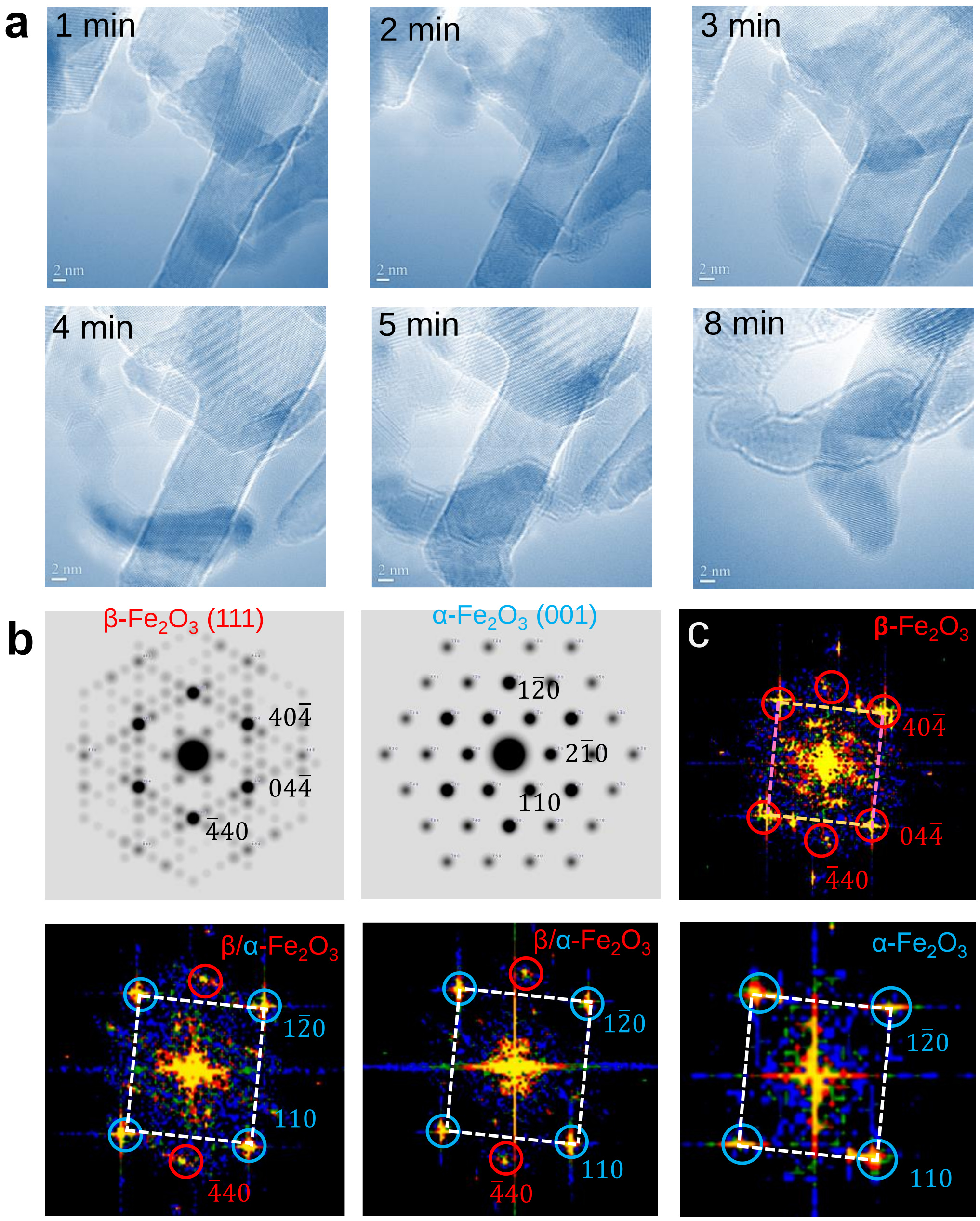

Supplementary Fig. 38 The phase transition and SAED diffraction patterns on β-Fe_2O_3 TSS after prolonged transmission electron microscopy electron beam irradiation. a, Observing the phase transition process of β-Fe_2O_3 from amorphous to holocrystalline β-Fe_2O_3 and then to crystalline α-Fe_2O_3 through continuous electron beam irradiation. **b**, Simulated electron diffraction pattern of Fe_2O_3. **c**, Observing the phase transition process of β-Fe_2O_3.

The structural evolution follows a controllable process, transitioning from holocrystalline β-Fe_2O_3 to amorphous β-Fe_2O_3, and back to holocrystalline β-Fe_2O_3 (Supplementary Figs. 32–37), as observed through a series of SAED evolution analyses (Supplementary Fig. 38). During the high energy electron beam exposure, the heat concentrated on the amorphous atomic layer triggers a phase transition, accompanied by the extension of amorphous whiskers attributed to the differential unit cell volumes between phases.

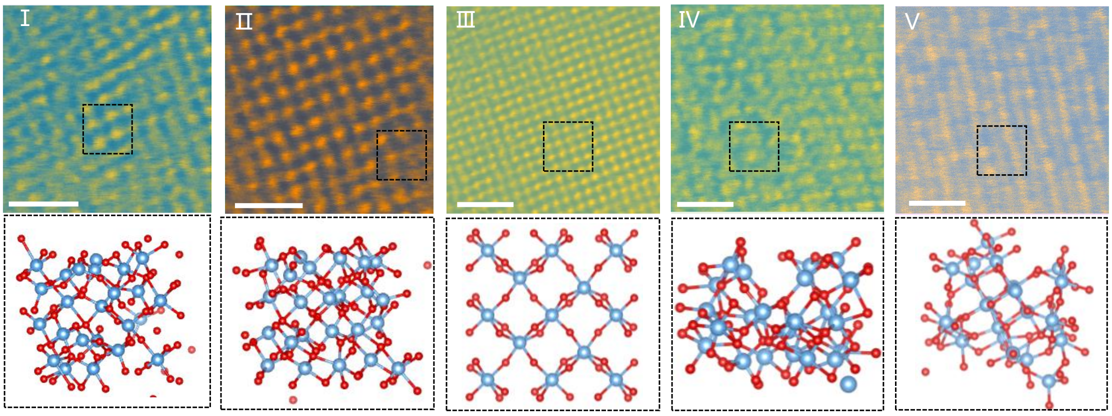

Supplementary Fig. 39 HAADF-STEM images of β-Fe_2O_3 TSS during phase transition. I, II and III represent short-range order, medium-range order and long-range order respectively. IV and V represent the blending order. Light blue and red balls represent iron atoms and oxygen atoms, respectively. Scale bar: 5 nm.

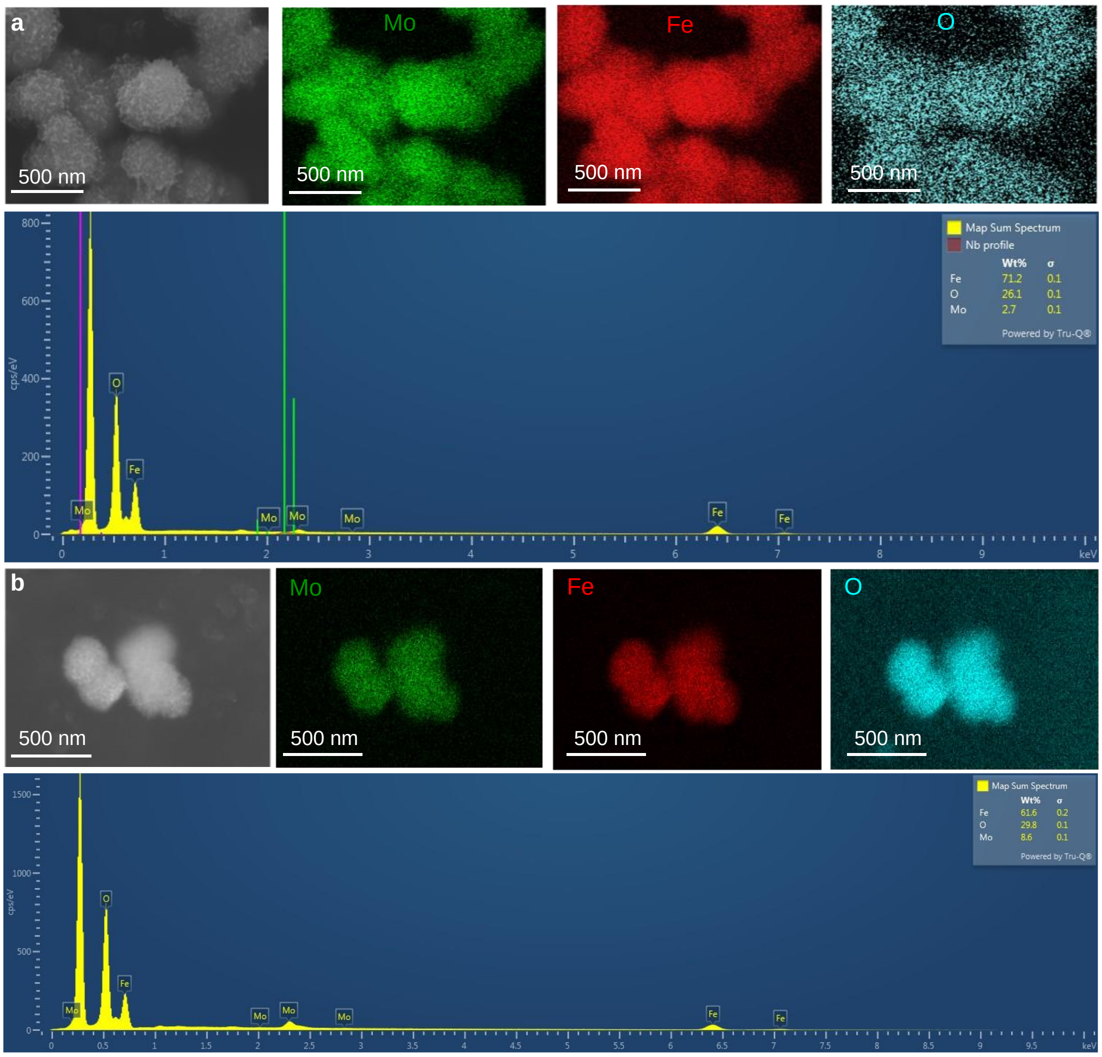

Supplementary Fig. 40 SEM images and corresponding EDX elemental mappings of 3 wt% $Mo_1/\beta\text{-}Fe_2O_3$ and 9 wt% $Mo_1/\beta\text{-}Fe_2O_3$. a, SEM images and corresponding EDX elemental mappings of 3 wt% $Mo_1/\beta\text{-}Fe_2O_3$. **b**, SEM images and corresponding EDX elemental mappings of 9 wt% $Mo_1/\beta\text{-}Fe_2O_3$.

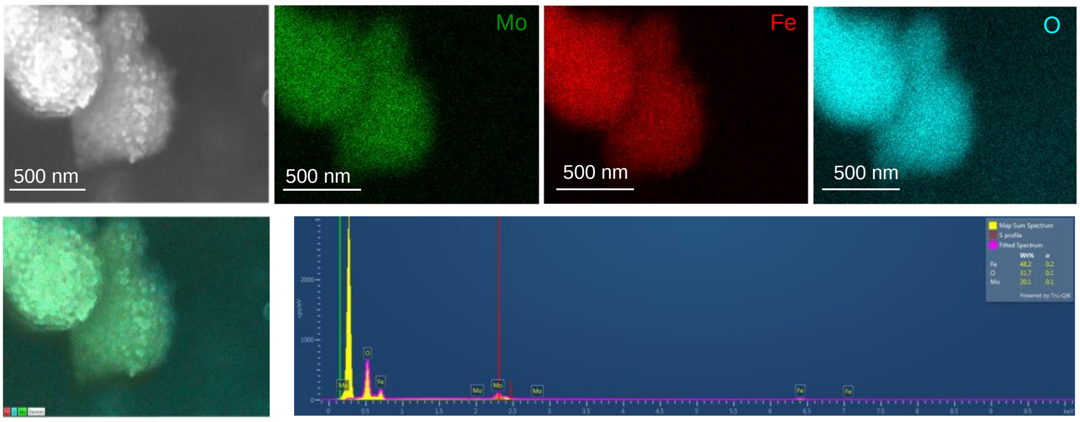

Supplementary Fig. 41 SEM images and corresponding EDX elemental mappings of 18 wt% $Mo_1/\beta\text{-}Fe_2O_3$.

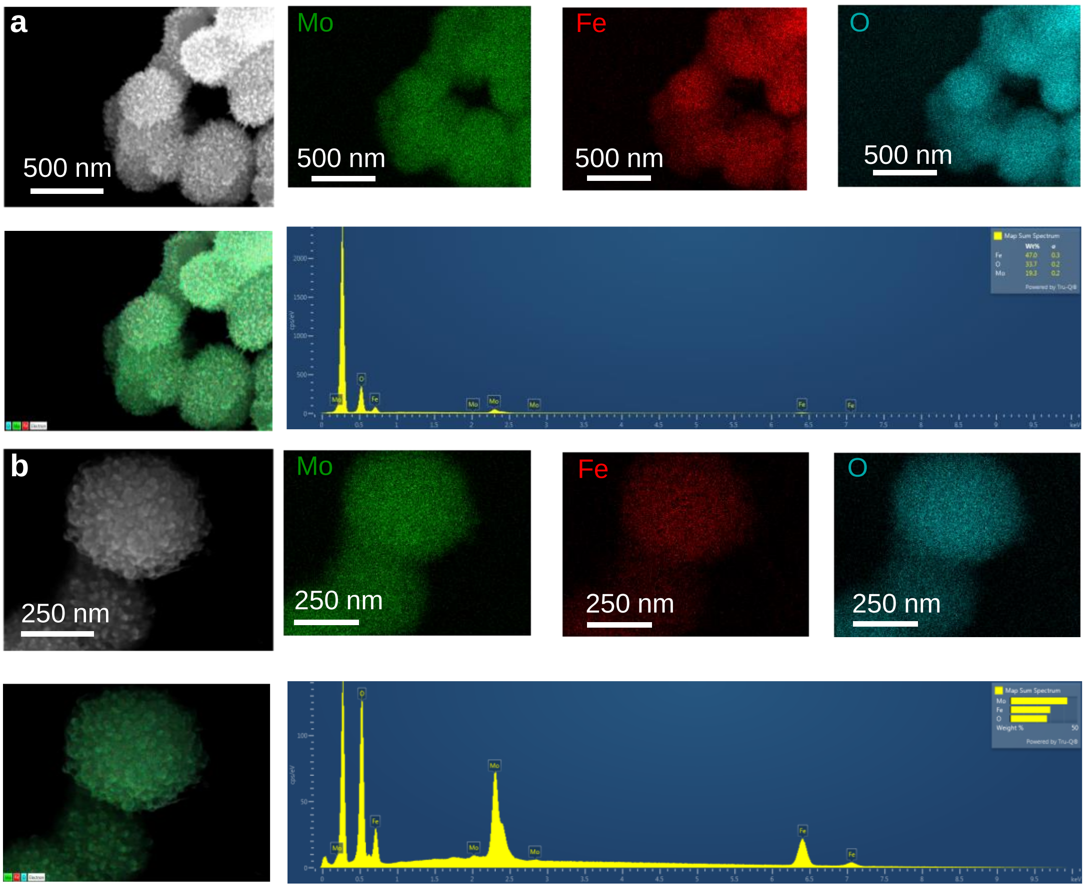

Supplementary Fig. 42 SEM images and corresponding EDX elemental mappings of 21 wt% Mo_1/β-Fe_2O_3. **a**, Low magnification SEM image and corresponding EDX elemental mappings of 21 wt% Mo_1/β-Fe_2O_3. **b**, High magnification SEM image and corresponding EDX elemental mappings of 21 wt% Mo_1/β-Fe_2O_3.

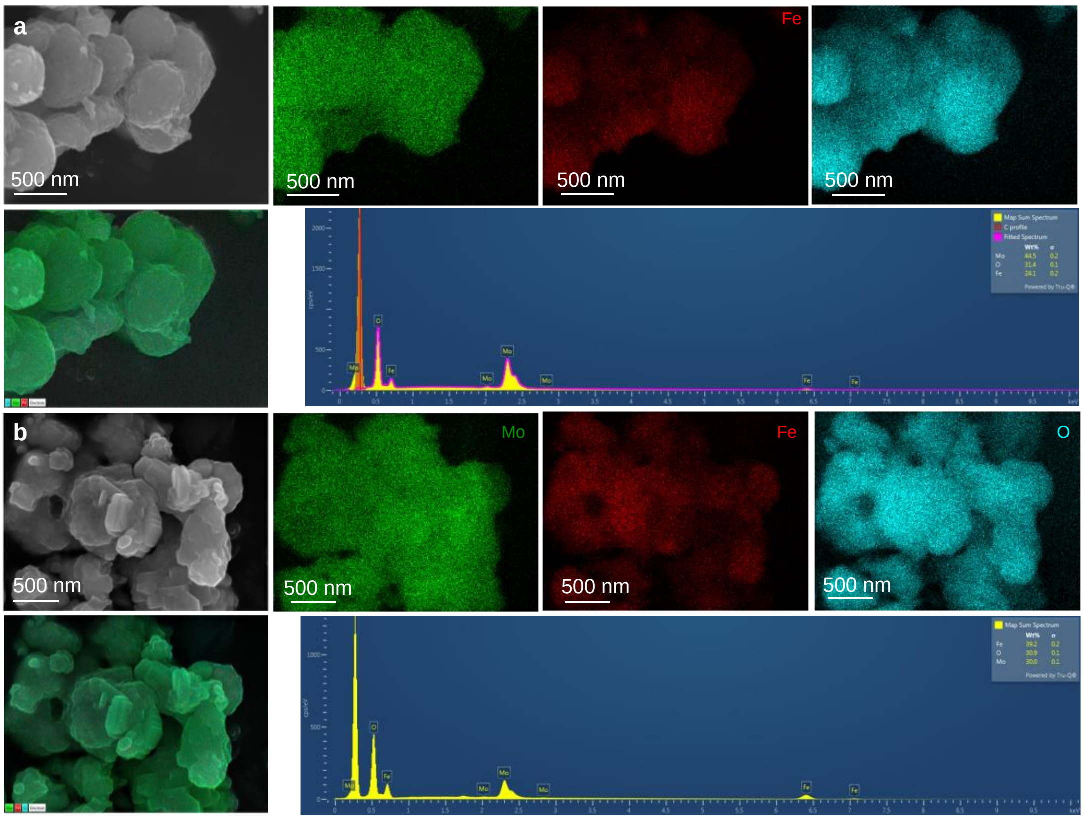

Supplementary Fig. 43 SEM images and corresponding EDX elemental mappings of 24 wt% Mo/β-Fe_2O_3 (MoO_3/β-Fe_2O_3) and 27 wt% Mo/β-Fe_2O_3 (MoO_3/β-Fe_2O_3). a, SEM images and corresponding EDX elemental mappings of 24 wt% Mo/β-Fe_2O_3 (MoO_3/β-Fe_2O_3). **b**, SEM images and corresponding EDX elemental mappings of 27 wt% Mo/β-Fe_2O_3 (MoO_3/β-Fe_2O_3).

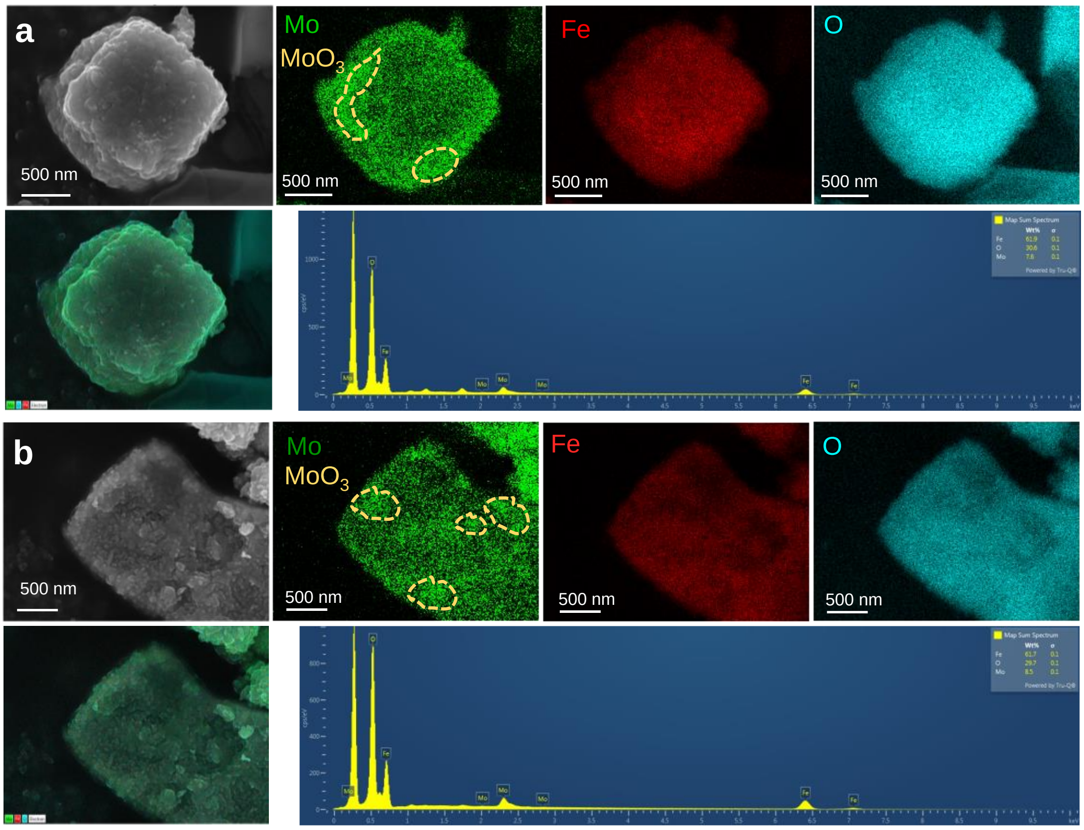

Supplementary Fig. 44 SEM images and corresponding EDX elemental mappings. a, SEM images and corresponding EDX elemental mappings of 6 wt% Mo/holocrystalline β-Fe_2O_3 (MoO_3/β-Fe_2O_3). **b**, SEM images and corresponding EDX elemental mappings of 9 wt% Mo/holocrystalline β-Fe_2O_3 (MoO_3/β-Fe_2O_3).

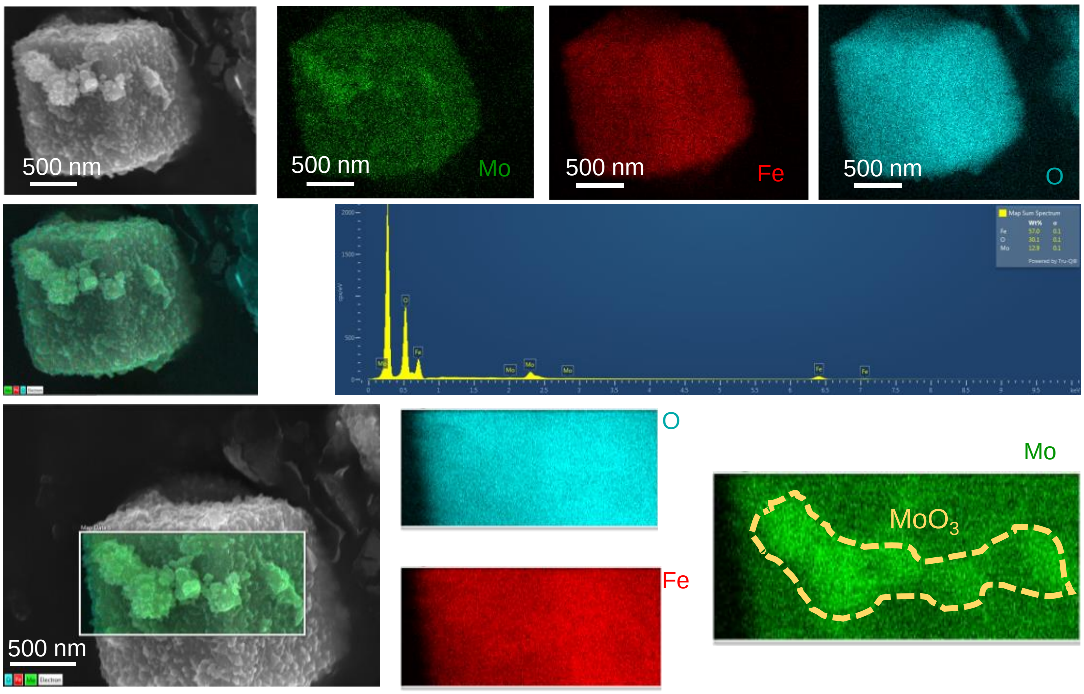

Supplementary Fig. 45 SEM images and corresponding EDX elemental mappings of 15 wt% Mo/holocrystalline β-Fe_2O_3 (MoO_3/β-Fe_2O_3).

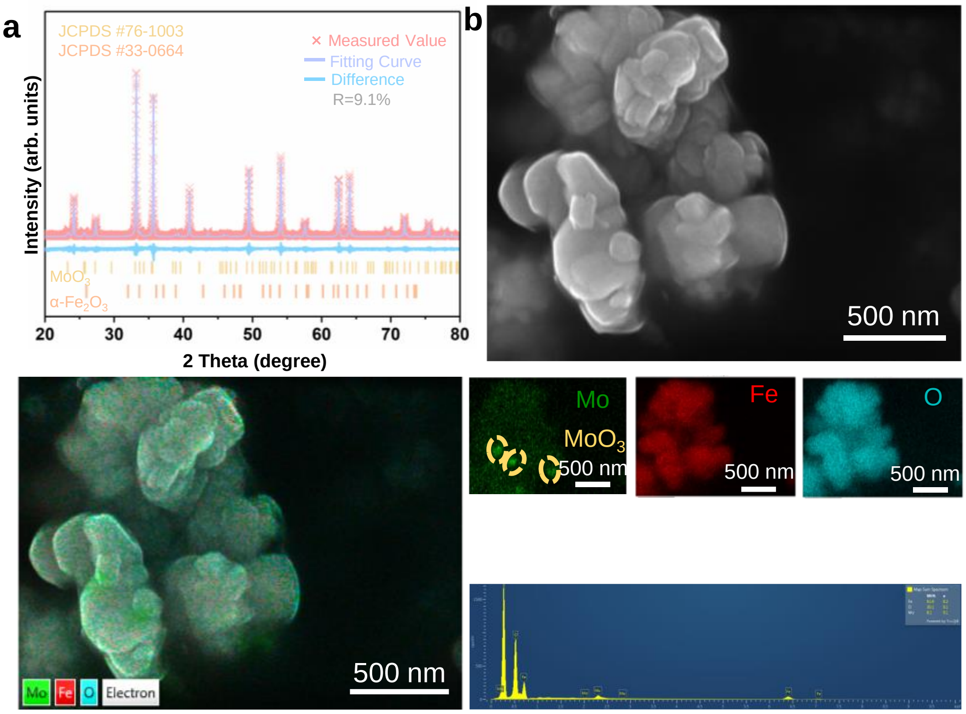

Supplementary Fig. 46 Rietveld refinement of XRD pattern, SEM images and corresponding EDX elemental mappings of 9 wt% Mo/holocrystalline α-Fe_2O_3 (MoO_3/β-Fe_2O_3). a, Rietveld refinement of XRD pattern of 9 wt% Mo/holocrystalline α-Fe_2O_3 (MoO_3/β-Fe_2O_3). **b**, SEM images and corresponding EDX elemental mappings of 9 wt% Mo/holocrystalline α-Fe_2O_3 (MoO_3/β-Fe_2O_3).

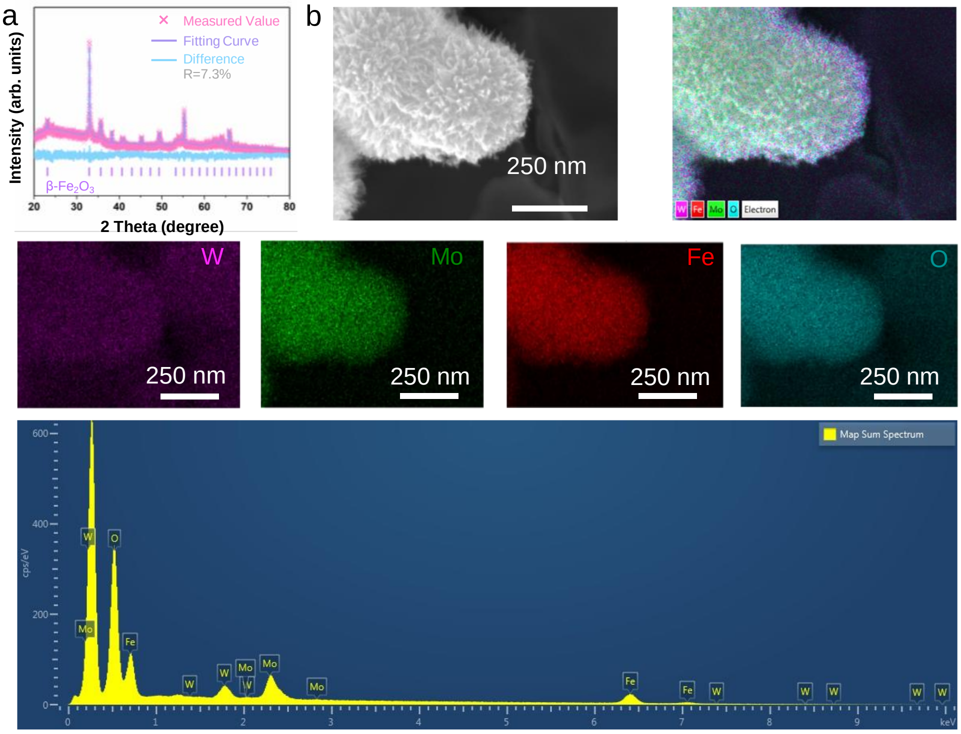

Supplementary Fig. 47 Rietveld refinement of XRD pattern, SEM images and corresponding EDX elemental mappings of 21 wt% $(MoW)_1/\beta\text{-}Fe_2O_3$. a, Rietveld refinement of XRD pattern of 21 wt% $(MoW)_1/\beta\text{-}Fe_2O_3$. **b**, SEM images and corresponding EDX elemental mappings of 21 wt% $(MoW)_1/\beta\text{-}Fe_2O_3$.

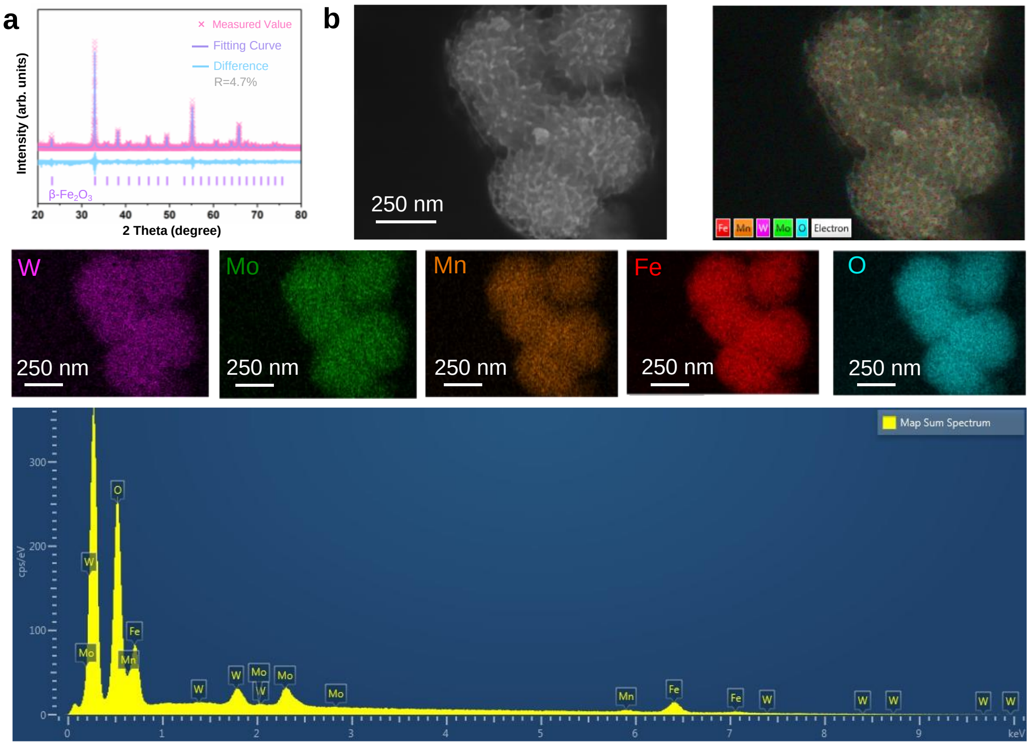

Supplementary Fig. 48 Rietveld refinement of XRD pattern, SEM images and corresponding EDX elemental mappings of 21 wt% $(MnMoW)_1/\beta\text{-}Fe_2O_3$. a, Rietveld refinement of XRD pattern of 21 wt% $(MnMoW)_1/\beta\text{-}Fe_2O_3$. **b**, SEM images and corresponding EDX elemental mappings of 21 wt% $(MnMoW)_1/\beta\text{-}Fe_2O_3$.

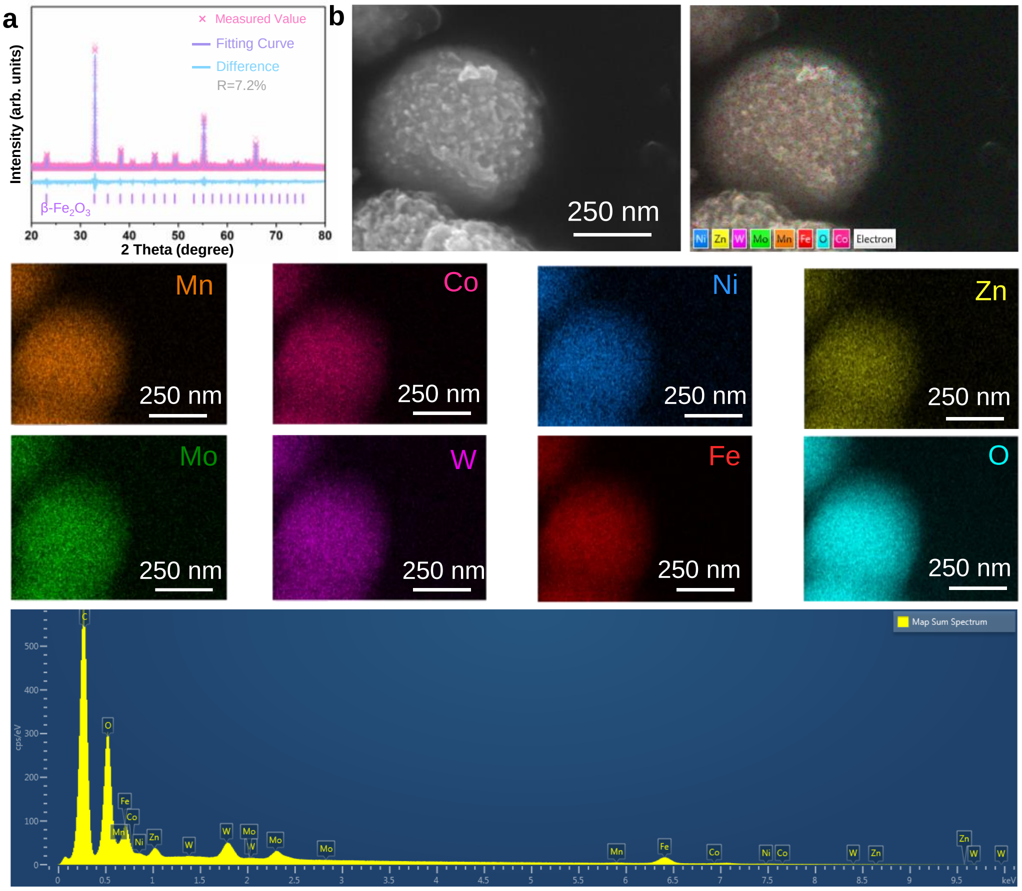

Supplementary Fig. 49 Rietveld refinement of XRD pattern, SEM images and corresponding EDX elemental mappings of HESA. a, Rietveld refinement of XRD pattern of 21 wt% $(MnCoNiZnMoW)_1/\beta\text{-}Fe_2O_3$. **b**, SEM images and corresponding EDX elemental mappings of 21 wt% $(MnCoNiZnMoW)_1/\beta\text{-}Fe_2O_3$.

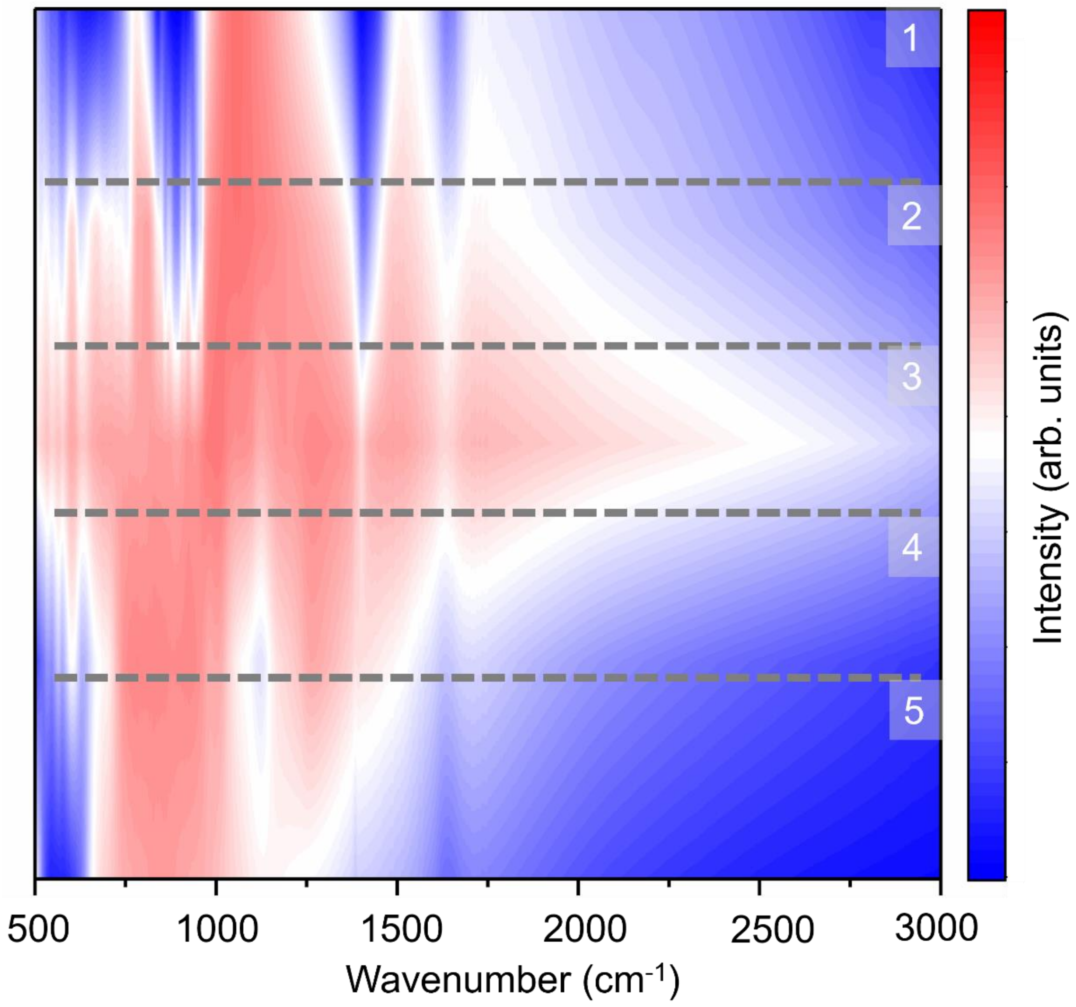

Supplementary Fig. 50 *Ex situ* IR spectroscopy of different samples under the same conditions. The 1, 2, 3, 4 and 5, represent $(NH_4)_2MoO_4{\cdot}4H_2O$, $(NH_4)_2MoO_4+H_2O$, β-Fe_2O_3 TSS, holocrystalline β-Fe_2O_3 and holocrystalline α-Fe_2O_3, respectively.

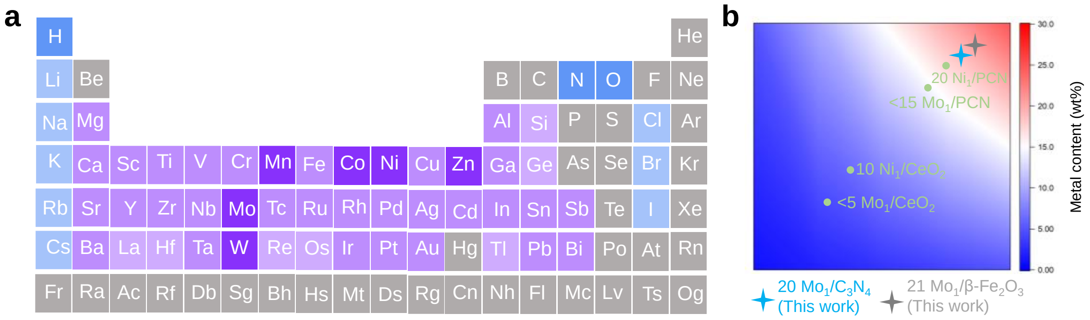

Supplementary Fig. 51 **a**, Periodic table showing elements involved in the formation of UDSA and alkali metal salts. Dark blue, NO_3^- and OH^-; Light blue, alkali metal salts; Light purple, exploring fewer single-atoms. Medium purple, exploring more single-atoms. Deep purple, UDSA verified by this work. **b**, Comparison of the metal content reported in the literature with our work.

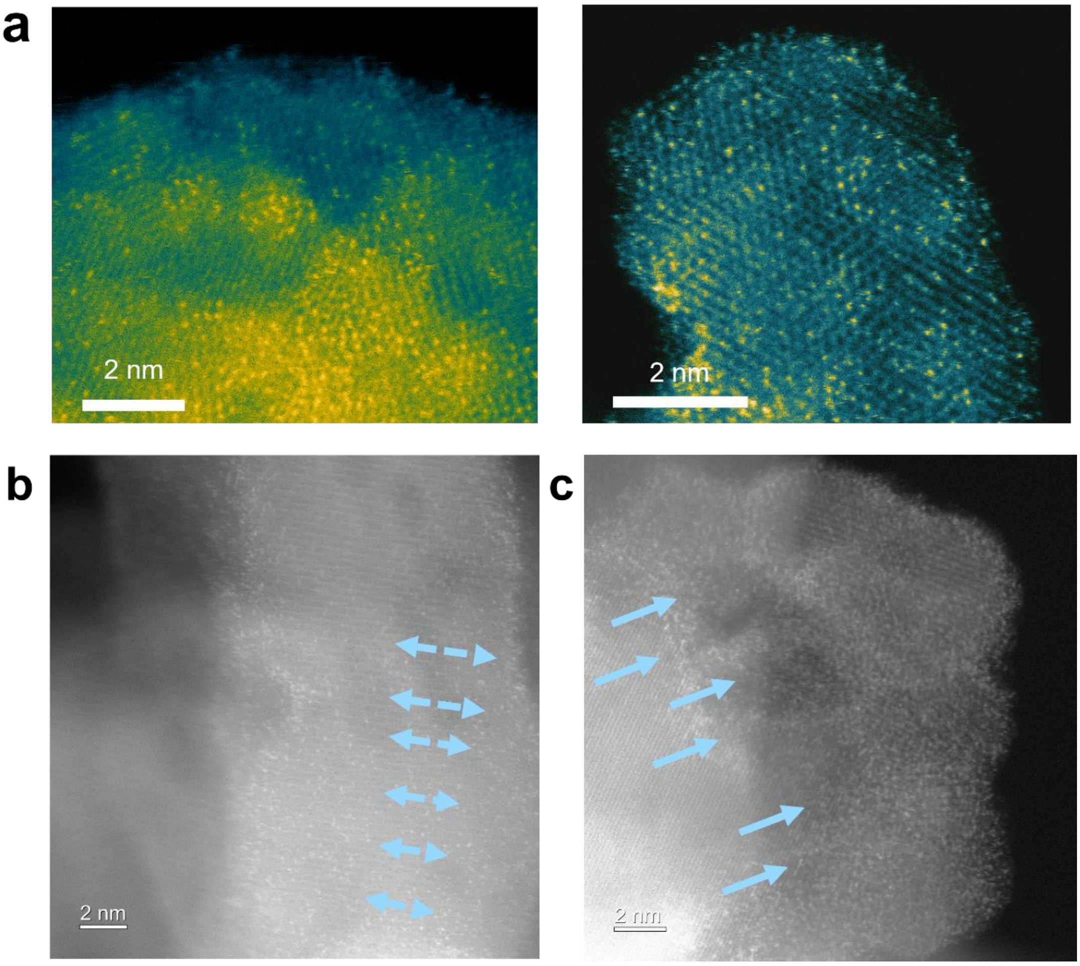

Supplementary Fig. 52 **a**, High saturation of Mo atoms on the TSS substrate observed by HAADF-STEM image. Low saturation of Mo on the holocrystalline structure observed by HAADF-STEM image. **b**, Direct observed HESA undergoes diffusion and migration across lattices in β-Fe_2O_3 TSS. **c,** Direct observed HESA undergoes diffusion, migration and sintering across lattices in holocrystalline β-Fe_2O_3.

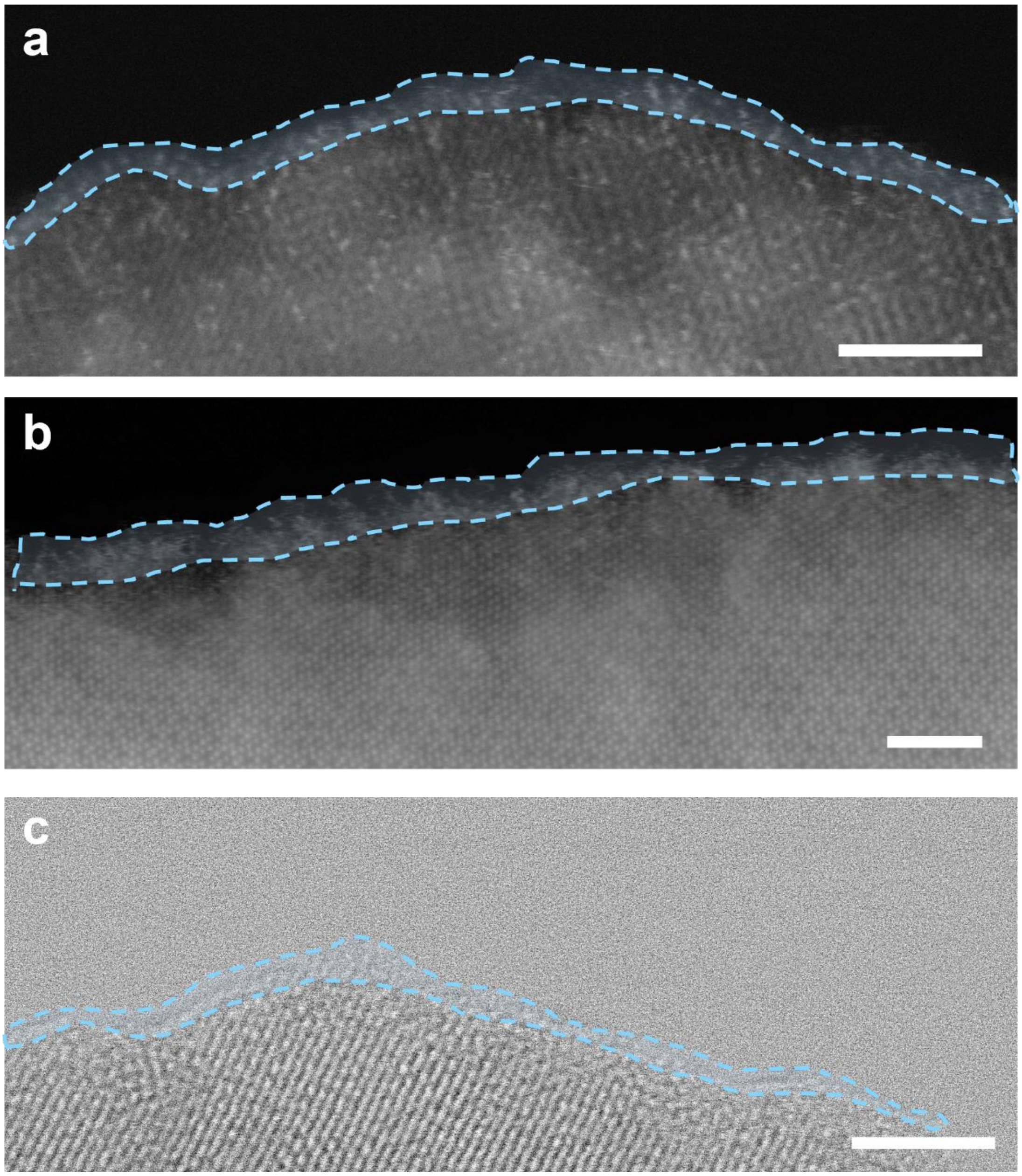

Supplementary Fig. 53 Observing the adsorbate-substrate interactions during growth process. a, Observing the layered coverage of heterogeneous atoms on the β-Fe_2O_3 TSS surface. **b**, Observing the formation of HESA on the surface of β-Fe_2O_3. **c**, Observing the layered coverage of HEM on the surface of β-Fe_2O_3. Scale bar, 2 nm.

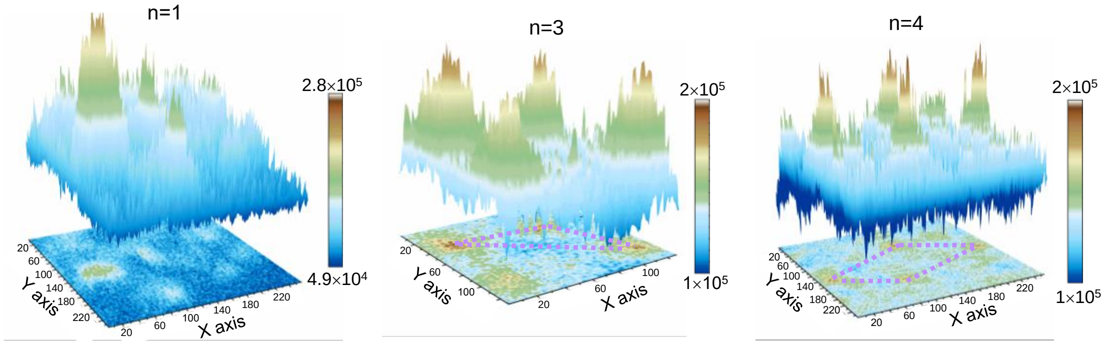

Supplementary Fig. 54 The observed atoms exist in the TSS lattice.

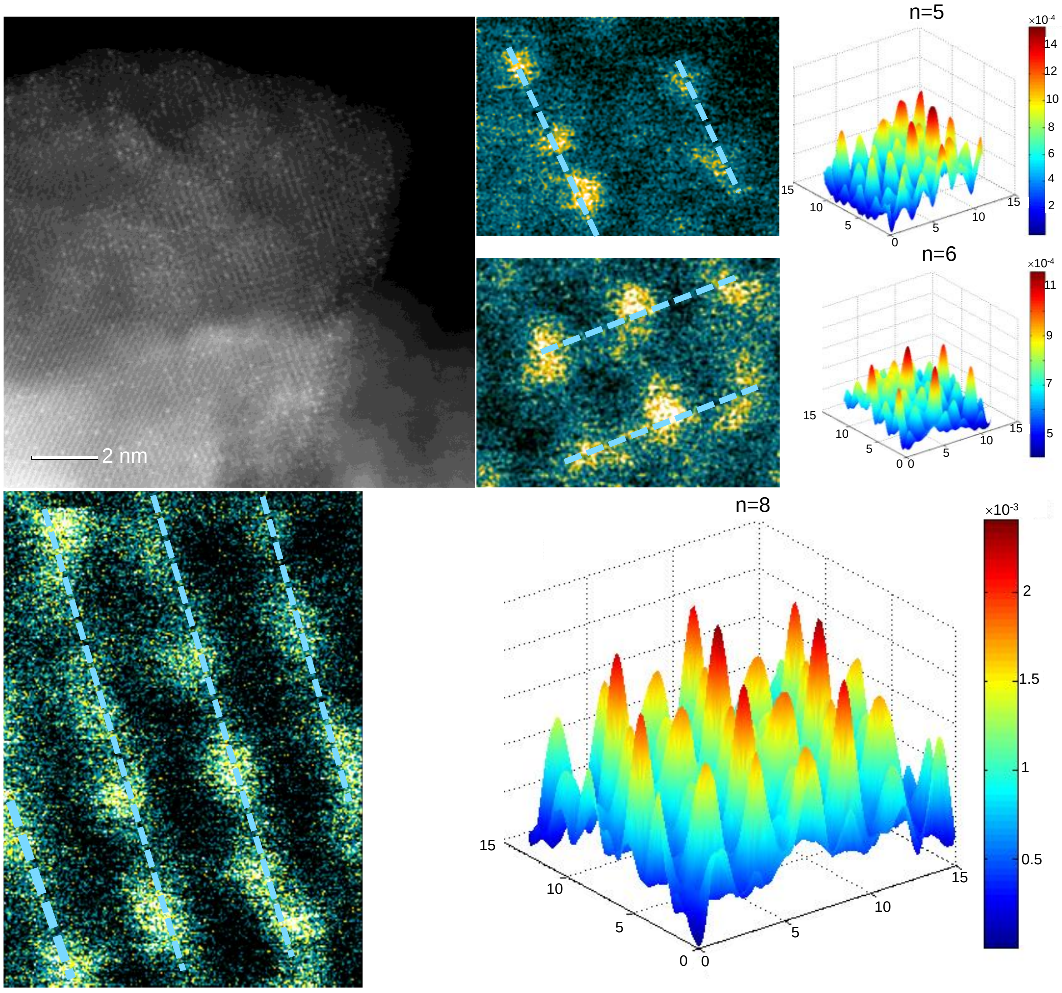

Supplementary Fig. 55 HAADF-STEM images of Mo$_1$/β-Fe$_2$O$_3$ and simulating the in-plane atomic attachment.

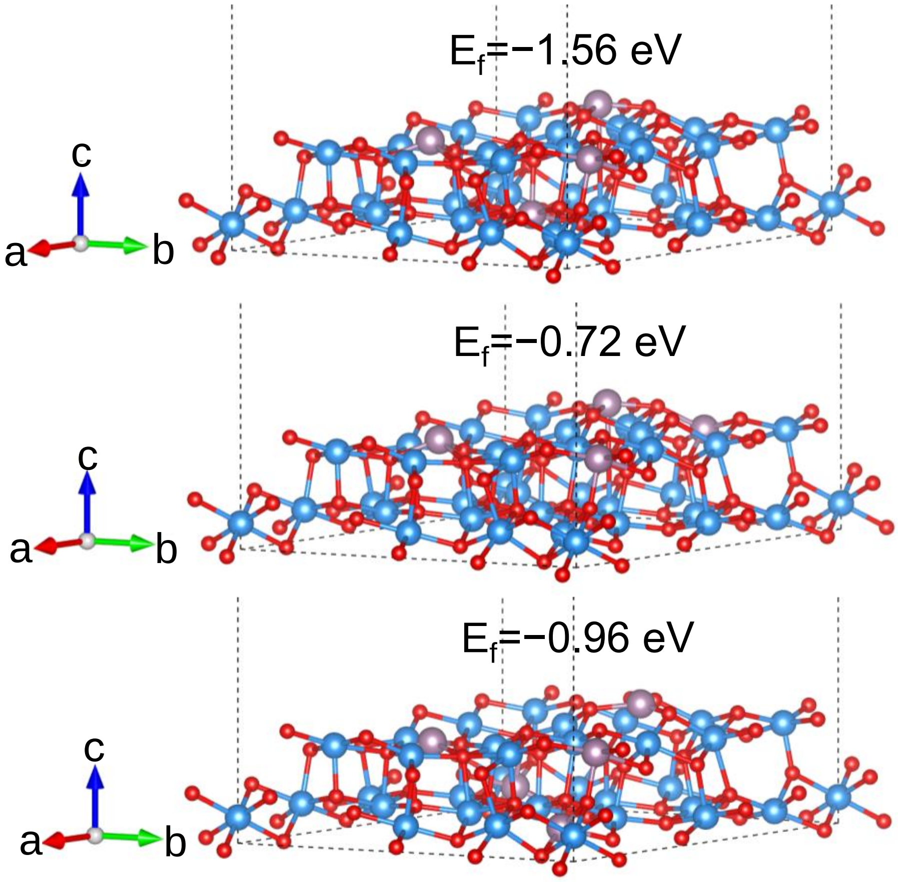

Supplementary Fig. 56 DFT-calculated formation energy of Mo dispersed on the β-Fe_2O_3 TSS substrate by nonclassical growth pathway.

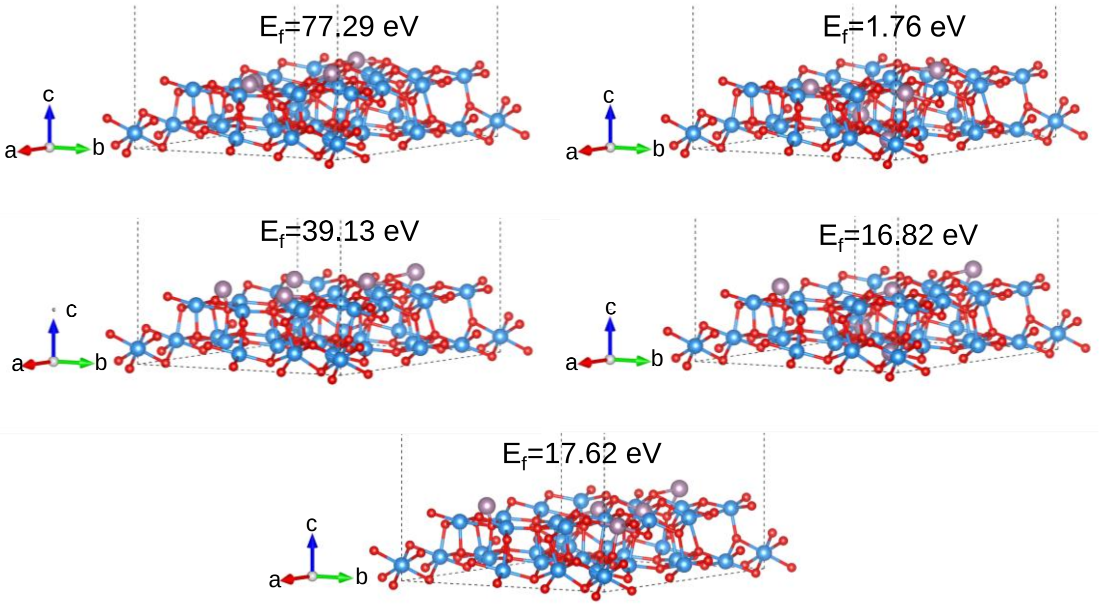

Supplementary Fig. 57 DFT-calculated formation energy of Mo dispersed on different positions of β-Fe_2O_3 TSS substrate by classical growth pathway.

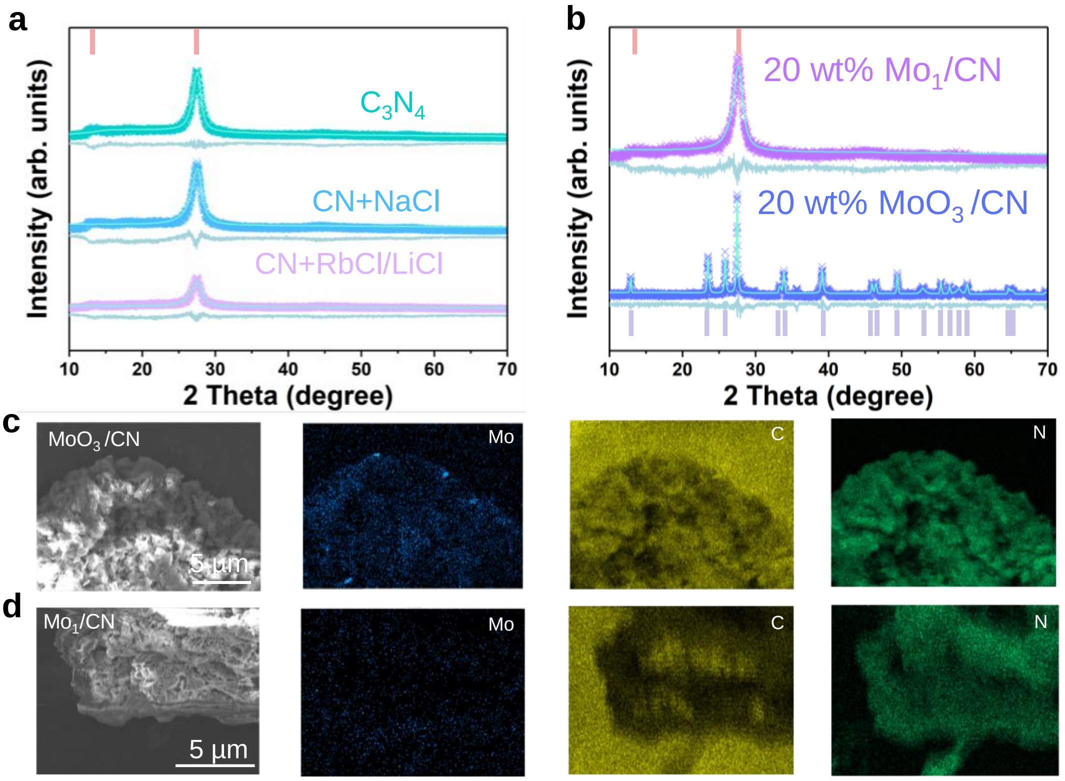

Supplementary Fig. 58 Rietveld refinement of XRD pattern, SEM images and corresponding EDX elemental mappings of samples. **a**, XRD patterns of C_3N_4 treated with different metal salts. **b**, XRD patterns of C_3N_4 TSS and holocrystalline C_3N_4 loaded with Mo atoms. **c**, SEM images and corresponding EDX elemental mappings of MoO_3/CN. **d**, SEM images and corresponding EDX elemental mappings of Mo_1/CN.

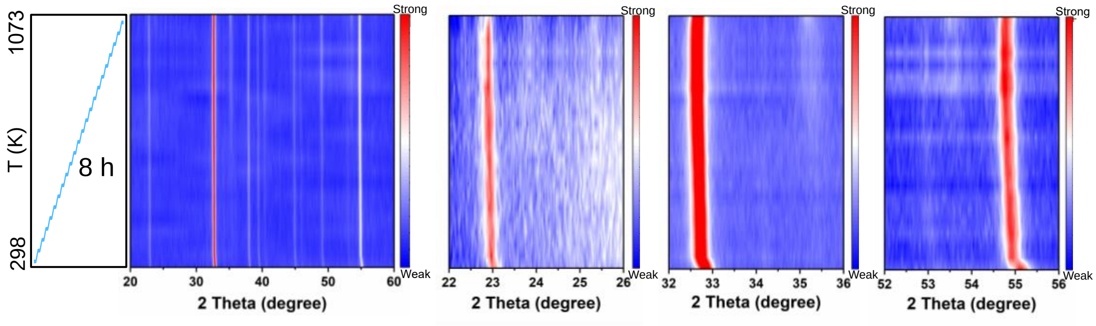

Supplementary Fig. 59 ***In situ*** **thermal stability of $Mo_1/\beta\text{-}Fe_2O_3$ by XRD.**

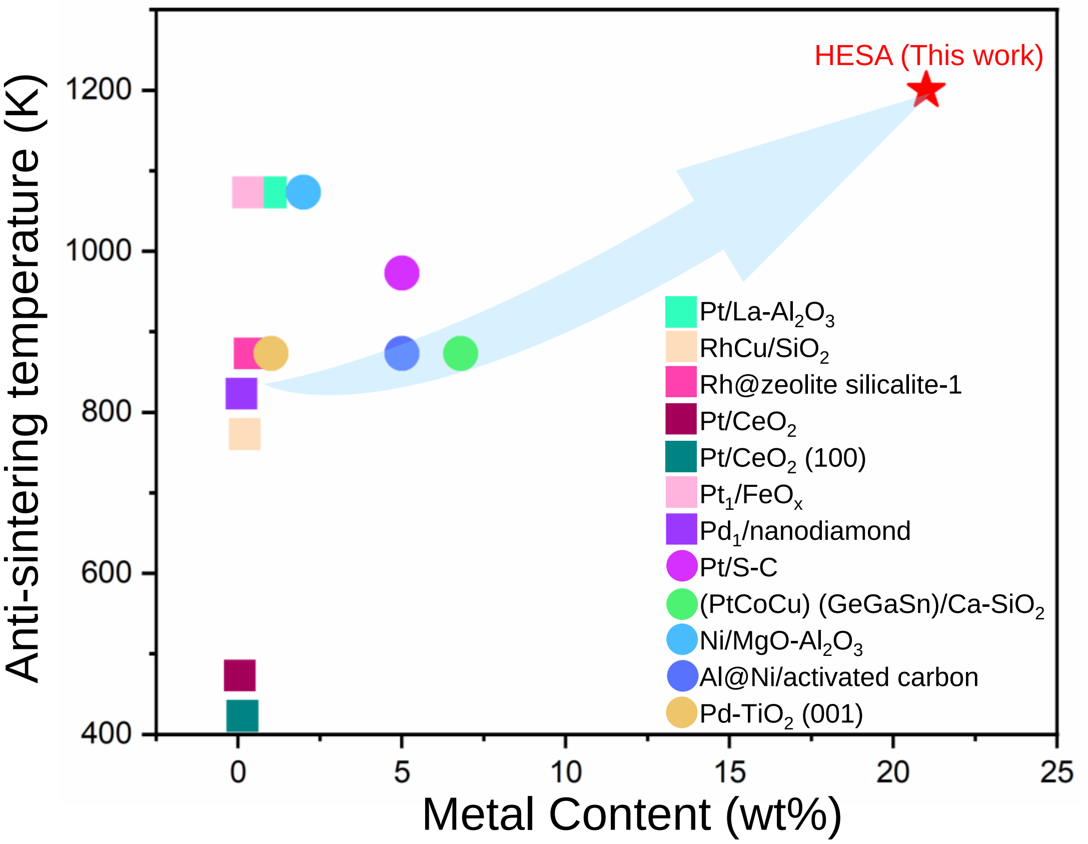

Supplementary Fig. 60 Comparison of HESA with reported anti-sintering temperatures and metal contents of heterogeneous metals.

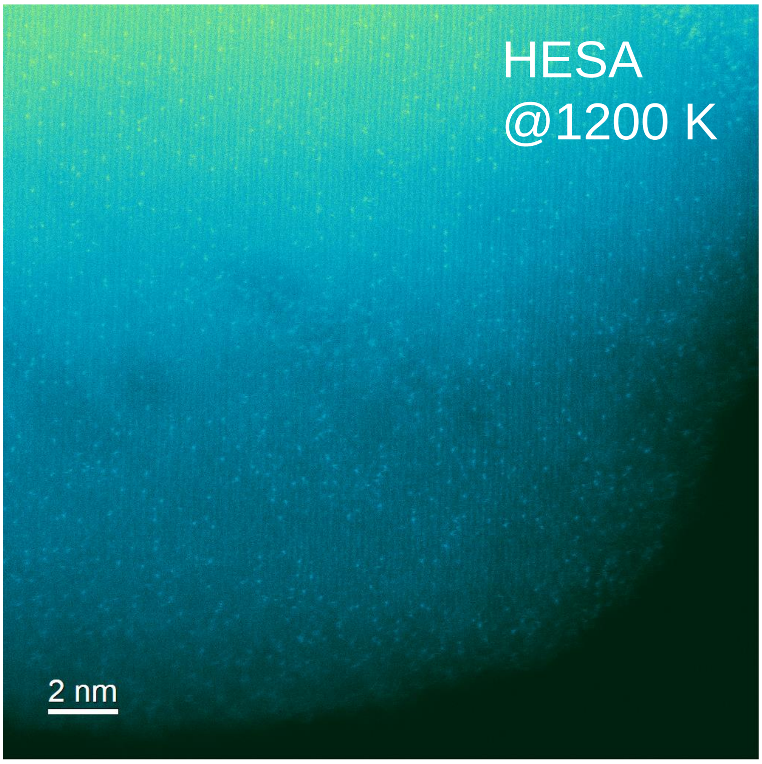

Supplementary Fig. 61 HAADF-STEM image for evaluating anti-sintering performance of HESA at 1200 K.

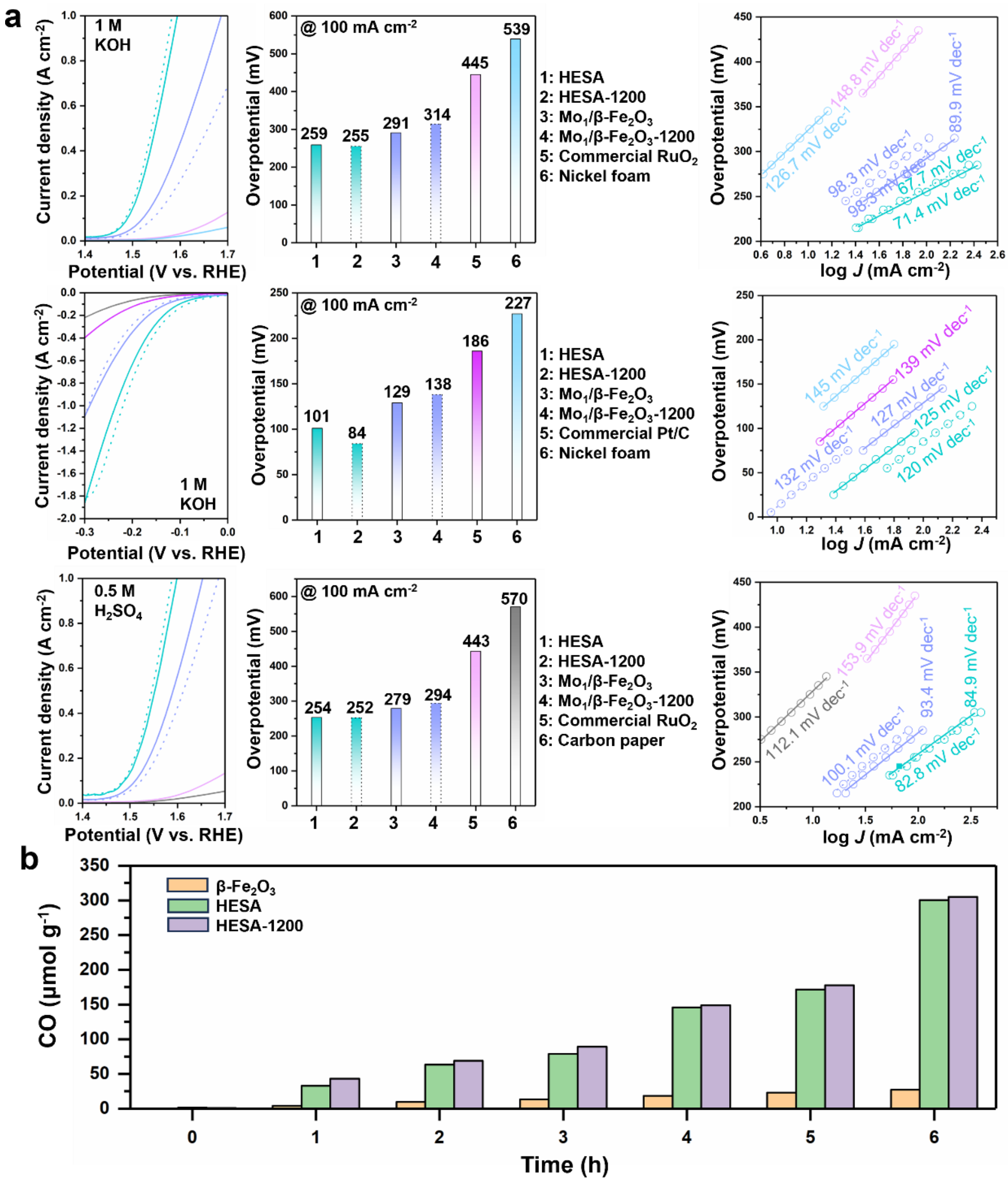

Supplementary Fig. 62 Application evaluation of HESA samples. a, Linear sweep voltammetry curves, overpotentials and Tafel plots for different samples. **b,** Photothermal CO_2 hydrogenation test.

Oxygen evolution and hydrogen evolution reaction measurements were carried out for the HESA and reference samples in 1.0 M KOH or 0.5 M H_2SO_4 electrolyte using a CHI660E electrochemical workstation. The experiments utilized a standard three-electrode cell, consisting of a working electrode, an Ag/AgCl reference electrode, and a graphite rod counter electrode in 1.0 M KOH electrolyte (a Pt foil counter electrode in 0.5 M H_2SO_4 electrolyte). The recorded potentials were corrected to the reversible hydrogen electrode (RHE) according to equation: $E_{RHE} = E_{Ag/AgCl} + E^0_{Ag/AgCl} + 0.059\ pH$. Where E_{RHE} and $E^0_{Ag/AgCl}$ are potentials versus RHE, with $E^0_{Ag/AgCl} = 0.1976$ V at 25 °C.

Photothermal CO_2 hydrogenation was conducted in a glass reactor with an area of 4.91 cm^2 according to the setup developed by our team[7]. The reaction was driven by a 300 W Xe lamp (PLS-SXE300, Perfectlight, China), serving as the light source to initiate the photothermal process. The light intensity incident on the sample surface was precisely measured using a high-precision optical power meter (PM100D, Thorlabs, USA), ensuring accurate control and reproducibility of the experimental conditions.

We examined overpotentials at current densities of 100 mA cm^{-2} and comparing with regular single-atom samples and commercial samples. Taking alkaline OER as a case, HESA exhibited an overpotential of only 259 mV, which is significantly lower than that of $Mo_1/\beta\text{-}Fe_2O_3$ and $Mo_1/\beta\text{-}Fe_2O_3$-1200, respectively. Meanwhile, the corresponding Tafel plot for HESA delivers a slope of only 71.4 mV dec^{-1}, indicating superior reaction kinetics. The HESA also showed a lower overpotential and faster kinetics in a three-electrode system in acidic media. Furthermore, our observations reveal that the properties of HESA samples remain largely unaffected by high-temperature treatment. In contrast, regular single-atom catalysts exhibit a notable decline in performance, primarily attributed to the loss of metal active sites. This degradation occurs as a result of formation of clusters or nanoparticles during high-temperature sintering, which diminishes the dispersion and availability of active sites in regular single-atom systems. These results demonstrate that OER and HER kinetics are significantly accelerated on HESA sample, with the catalytic activity exhibiting a strong dependence on the entropy of metal atoms. Additionally, HESA maintains high thermodynamic stability in photothermal catalysis (**Supplementary Fig. 62b**).

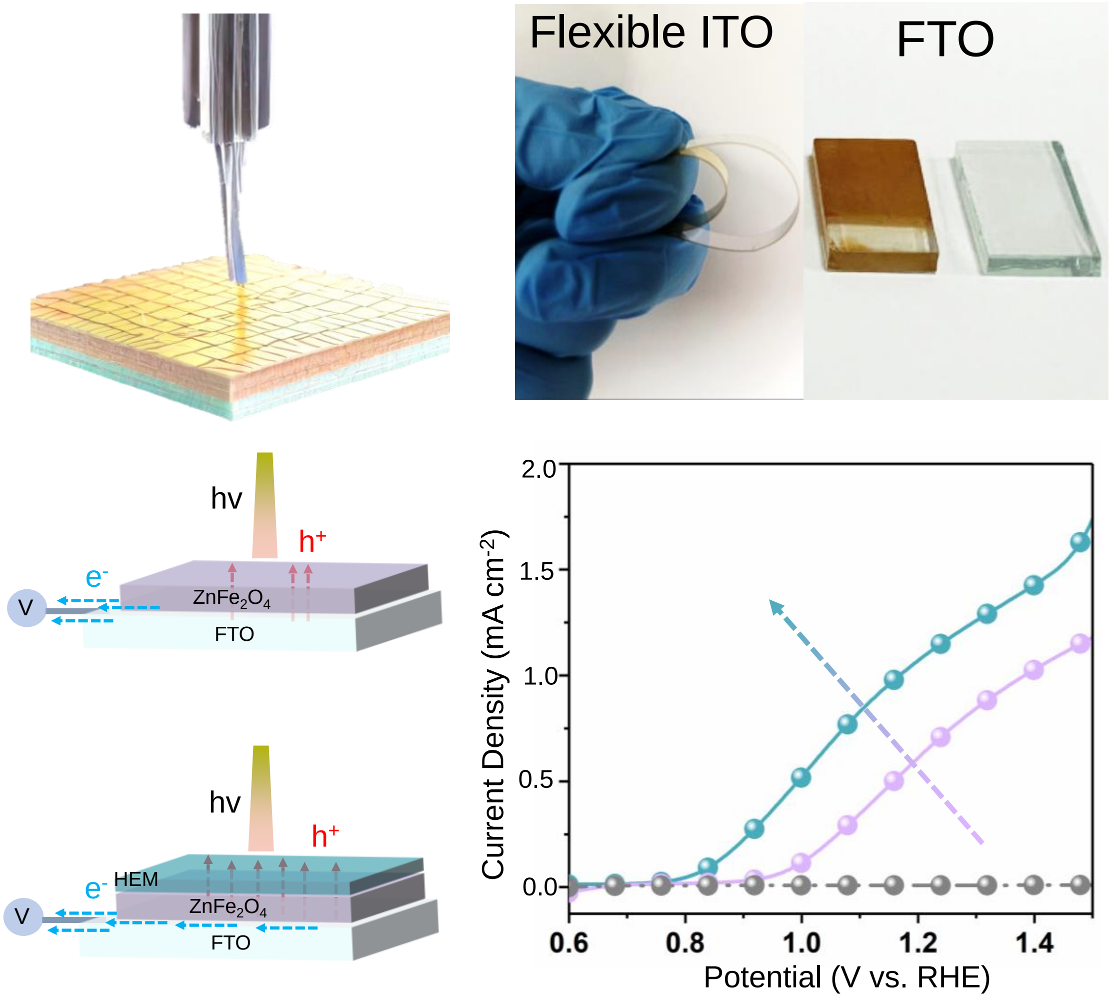

Supplementary Fig. 63 Using HEM as ink coating or printing on different substrates as electronics instead of traditional materials. Using HEM as ink coating or printing on substrates as electronics instead of traditional materials. Linear sweep voltammograms of n-type $ZnFe_2O_4$ coated with HEM ink under dark and AM1.5G illumination conditions. The overpotential of n-type $ZnFe_2O_4$ was significantly reduced by 150 mV. Reducing contact loss and charge transport resistance between solid-liquid interfaces using HEM to accelerate the kinetic process.

Supplementary Table 1. Electronegativity and atomic radius.

Element	Electronegativity	Atomic Radius (nm)
Mg	1.31	0.160
Al	1.61	0.143
Ti	1.54	0.147
V	1.63	0.131
Cr	1.66	0.125
Mn	1.55	0.130
Fe	1.83	0.124
Co	1.88	0.125
Ni	1.91	0.125
Cu	1.90	0.128
Zn	1.65	0.137
Ga	1.81	0.122
Ge	2.01	0.122
Y	1.22	0.181
Zr	1.33	0.160
Nb	1.60	0.143
Mo	2.16	0.136
In	1.78	0.162
Sn	1.96	0.155
Sb	2.05	0.145
Hf	1.30	0.159
Ta	1.50	0.143
W	2.36	0.137

Supplementary Table 2. Composition of different materials structure obtained from Materials Project.

Isomers	Name	Structure	Predicted Formation Energy (eV/atom)	Space Group	Number of Atoms
Fe_2O_3	β	Cubic	-1.637	$Ia\bar{3}$	80
	α	Trigonal	-1.708	$R\bar{3}c$	30
	α	Trigonal	-1.2	$P3$	30
C_3N_4	/	Hexagonal	0.112	$P\bar{6}m2$	14
	/	Cubic	1.512	$Fd\bar{3}m1$	56
	/	Cubic	0.503	$I\bar{4}3d$	28
	/	Cubic	0.498	$P\bar{4}3m$	7
	/	Hexagonal	2.384	$P\bar{6}$	7
	/	Hexagonal	0.585	$P6_3/m$	14
TiO_2	Anase	Tetragonal	-3.496	$I4_1/amd$	12
	Rutile	Tetragonal	-3.465	$P4_2/mnm$	6
	Brookite	Orthorhombic	-3.385	$Pbca$	24
In_2O_3	/	Cubic	-1.998	$Ia\bar{3}$	80
	/	Hexagonal	-1.968	$R\bar{3}c$	30
MoC	/	Hexagonal	-0.083	$P\bar{6}m2$	2
	/	Cubic	0.214	$Fm\bar{3}m$	8
BN	/	Hexagonal	-1.457	$P\bar{6}m2$	4
	/	Cubic	-1.384	$F\bar{4}3m$	8
	/	Hexagonal	-1.458	$P6_3/mmc$	4
	/	Hexagonal	-1.367	$P6_3mc$	4
	/	Orthorhombic	-1.16	$Imm2$	12
$YFeO_3$	/	Hexagonal	-2.831	$P6_3/mmc$	20
	/	Hexagonal	-2.826	$P6_3cm$	30
	/	cubic	-2.499	$Pm\bar{3}m$	5
MoS_2	/	Hexagonal	-1.202	$P6_3/mmc$	6
	/	Trigonal	-1.2	$R3m$	9
	/	Trigonal	-0.92	$R\bar{3}m$	9
	/	cubic	-0.934	$F\bar{4}3m$	48
	/	Hexagonal	-1.2	$P\bar{6}m2$	3
WP_2	β	Orthorhombic	-0.378	$Cmc21$	12
	α	Monoclinic	-0.363	$C2/m$	12
Al_2O_3	/	Cubic	-3.398	$Ia\bar{3}$	80
	/	Trigonal	-3.4	$R\bar{3}c$	30
	/	Orthorhombic	-3.38	$Pbca$	40
	/	Monoclinic	-3.374	$C2/m$	20
$CsPbBr_3$	/	Cubic	-1.678	$Pm\bar{3}m$	5
	/	Orthorhombic	-1.687	$Pnma$	20
ZnO	/	Hexagonal	-1.792	$P6_3mc$	4

	/	Cubic	-1.644	$Fm\bar{3}m$	8
	/	Cubic	-1.074	$Pm\bar{3}m$	2
	/	Hexagonal	-1.568	$P6_3/mmc$	4
NiP_2	/	Cubic	-0.372	$Pa\bar{3}$	12
	/	Monoclinic	-0.361	$C2/c$	12
$BiVO_4$	/	Tetragonal	-2.144	$I4_1/a$	24
	/	Tetragonal	-2.16	$I4_1/amd$	24
	/	Monoclinic	-2.101	$C2$	6
	/	Monoclinic	-2.086	$C2/c$	24
$InCuS_2$	/	Tetragonal	-0.7	$I\bar{4}2d$	16
	/	Trigonal	-6.56	$P3m1$	4
	/	Trigonal	-0.648	$R3m$	12
Ti_2C	/	Cubic	-0.643	$Fd\bar{3}m$	48
	/	Trigonal	-0.634	$R\bar{3}m$	9

Supplementary Table 3. Summary of sintering temperature for different samples.

Samples	**Composition**	**Sintering temperature (K)**	**Ref.**
Single-atoms	HESA	1200	This work
	Pt/La-Al_2O_3	1073	8
	RhCu/SiO_2	773	9
	Rh@zeolite silicalite-1	873	10
	Pt/CeO_2	473	11
	Pt/CeO_2 (100)	423	12
	Pt_1/FeO_x	1073	13
	Pd_1/nanodiamond	823	14
Clusters and nanoparticles	Pt/S-C	973	15
	(PtCoCu) (GeGaSn)/Ca-SiO_2	873	16
	Ni/MgO- Al_2O_3	1073	17
	Al@Ni/Activated carbon	873	18
	Pd-TiO_2 (001)	873	19

Supplementary Table 4. Atomic position coordinates before and after simulation.

Atomic number	**Before**			**After**		
	X	**Y**	**Z**	**X**	**Y**	**Z**
1	7.2735	0.369106	21.50226	9.250386	1.09159	21.83025
2	2.055394	2.4245	23.82198	3.443623	2.522807	24.76409
3	6.904394	7.2735	19.1828	9.842896	8.422726	20.04525
4	0	7.2735	21.50226	2.388076	8.035264	22.24602
5	2.4245	9.328894	21.50226	4.366433	10.09103	22.47487
6	7.642606	7.2735	23.82198	8.272449	8.891376	24.67578
7	2.793606	2.4245	19.1828	4.758433	2.934603	19.75102
8	0	2.4245	21.50226	1.991229	3.394184	22.292
9	2.4245	4.479894	21.50226	4.787024	5.526183	21.37974
10	6.904394	2.4245	23.82198	8.247139	4.287078	25.383
11	2.055394	7.2735	19.1828	5.344836	7.695202	19.37098
12	4.849	7.2735	21.50226	7.141596	8.189336	21.95598
13	7.2735	5.218106	21.50226	9.453352	5.990668	22.59887
14	2.793606	7.2735	23.82198	3.487066	8.170963	25.44533
15	7.642606	2.4245	19.1828	10.35274	3.719039	19.11578
16	4.849	2.4245	21.50226	7.027492	3.628643	22.28986
17	0	0	18.82972	2.16619	0.846605	20.4073
18	4.849	4.849	18.82972	7.87426	5.823325	19.95824
19	4.849	0	24.17506	6.179331	1.865183	25.3894
20	0	4.849	24.17506	0.591647	6.981047	25.24138
21	4.849	4.849	23.4689	6.084128	6.128394	24.23775
22	0	0	23.4689	1.621496	0.704856	23.79793
23	0	4.849	19.53588	2.446693	5.658192	20.60064
24	4.849	0	19.53588	6.87847	1.110979	20.16942

Supplementary Table 5. The elemental weight percentages in different samples determined by ICP-AES.

Sample	Mo (wt%) First	Mo (wt%) Second	Mo (wt%) Third
3 wt% $Mo_1/\beta\text{-}Fe_2O_3$	2.7	2.6	2.3
9 wt% $Mo_1/\beta\text{-}Fe_2O_3$	7.9	8.3	8.2
21 wt% $Mo_1/\beta\text{-}Fe_2O_3$	19.3	22.8	21.3
20 wt% Mo_1/C_3N_4	19.2	19.5	19.1

Supplementary Table 6. Fitting parameters of Mo K-edge, Zn K-edge and W L$_3$-edge EXAFS spectra.

Sample	Path	R (Å)	CN	$\sigma^2\times10^{-3}$(Å^2)	R factor
21 wt% Mo$_1$/β-Fe$_2$O$_3$	Mo-O	1.65	5	0.00176	0.018
Mo foil	Mo-Mo1	2.72	8	0.003	0.018
	Mo-Mo2	3.13	6	0.004	
	Mo-Mo3	4.45	12	0.007	
Zn foil	Zn-Zn1	2.66	6	0.01	0.02
	Zn-Zn2	2.89	6	0.007	
	Zn-Zn3	3.9	6	0.015	
W foil	W-W1	2.74	8	0.003	0.006
	W-W2	3.15	6	0.003	
MnCoNiZnMoW (HEM)	Mo-Mo1	2.80	8	0.009	0.013
	Mo-Mo2	3.21	5.02	0.006	
	Mo-Mo3	4.60	10.2	0.01	
	Mo-Zn0.1 (ZnMo$_3$)	3.13	4	0.006	
	Mo-Zn1.2 (ZnMo$_3$)	3.90	0.1	0.006	
	Mo-Zn0.1 (Zn$_6$Mo)	2.64	12	0.01	
	W-W1	2.28	8	0.006	0.018
	W-W2	3.08	8.8	0.006	
	W-W3	4.43	3.9	0.0003	
	W-W1.1 (MoW$_{11}$)	2.72	1.4	0.015	
	W-W3.1 (MoW$_{11}$)	2.28	6.8	0.007	
	W-Mo0.2 (MoW11)	3.63	0.1	0.015	
	Zn-Zn1	2.60	0.1	0.003	0.02
	Zn-Zn2	2.69	6	0.02	
	Zn-Zn3	3.92	6	0.015	
	Zn-W1	2.31	1.1	0.015	
	Zn-Mo1.1 (ZnMo$_3$)	2.88	0.6	0.008	

Note: For the Mo K-edge in Mo foil, S_0^2 was fixed at 0.965. ΔE_0 was refined as a global fit parameter, yielding a value of (-7.0±1.3) eV. Data ranges: $3 \leqslant k \leqslant 12$, $1.0 \leqslant R \leqslant 4.5$ Å. The distances for Mo-Mo are derived from the crystal structure of Mo metal. The distance of Mo-Mo is also obtained from the FEFF file of Mo metal. These coordination numbers were constrained based on the crystal stricture.

For the Mo K-edge in HEM, S_0^2 was fixed at 0.965. ΔE_0 was refined as a global fit parameter, yielding a value of (7.7±1.5) eV. Data ranges: $3 \leqslant k \leqslant 12$, $1.0 \leqslant R \leqslant 4.5$ Å. The distances for Mo-Mo and Mo-Zn are derived from the crystal structure of Mo metal, ZnMo$_3$ and Zn$_6$Mo. The distance of Mo-Mo is also obtained from the FEFF file of Mo metal, $ZnMo_3$ and Zn_6Mo. These coordination numbers were constrained based on the crystal stricture.

For the W L_3-edge in W foil, S_0^2 was fixed at 0.90. ΔE_0 was refined as a global fit parameter, yielding a value of (5.6±0.8) eV. Data ranges: $3 \leqslant k \leqslant 15$, $1.0 \leqslant R \leqslant 3$ Å. The distances for W-W and Mo-W are derived from the crystal structure of W metal. The distance of W-W and Mo-W is also obtained from the FEFF file of W metal. These coordination numbers were constrained based on the crystal stricture.

For the W L_3-edge in HEM, S_0^2 was fixed at 0.90. ΔE_0 was refined as a global fit parameter, yielding a value of (7.7±1.3) eV. Data ranges: $3 \leqslant k \leqslant 12$, $1.0 \leqslant R \leqslant 4.5$ Å. The distances for W-W and Mo-W are derived from the crystal structure of W metal and MoW_{11}. The distance of W-W and Mo-W is also obtained from the FEFF file of W metal and MoW_{11}. These coordination numbers were constrained based on the crystal stricture.

For the Zn K-edge in Zn foil, S_0^2 was fixed at 0.96. ΔE_0 was refined as a global fit parameter, yielding a value of (1.4±0.9) eV. Data ranges: $3 \leqslant k \leqslant 12.5$, $1.0 \leqslant R \leqslant 4$ Å. The distances for Zn-Zn are derived from the crystal structure of Zn metal. The distance of Zn-Zn is also obtained from the FEFF file of Zn metal. These coordination numbers were constrained based on the crystal stricture.

For the Zn K-edge in HEM, S_0^2 was fixed at 0.96. ΔE_0 was refined as a global fit parameter, yielding a value of (3.7±1.7) eV. Data ranges: $3 \leqslant k \leqslant 12.5$, $1.0 \leqslant R \leqslant 5$ Å. The distances for Zn-Zn are derived from the crystal structure of Zn metal and $ZnMo_3$. The distance of Zn-Zn is also obtained from the FEFF file of Zn metal and $ZnMo_3$. These coordination numbers were constrained based on the crystal stricture.

References

1. Zhu, G. *et al.* Self-similar mesocrystals form via interface-driven nucleation and assembly. *Nature* **590**, 416–422 (2021)
2. Jeon, S. *et al.* Reversible disorder-order transitions in atomic crystal nucleation. *Science* **371**, 498–503 (2021)
3. L. Gránásy, G. I. Tóth, J. A. Warren, F. Podmaniczky, G. Tegze, L. Rátkai, T. Pusztai, Phase-field modeling of crystal nucleation in undercooled liquids-a review. *Progress in Materials Science* **106**, 100569 (2019)
4. T. T. B. Vo, J. Lim, S. H. Joo, H. Kim, T. Lee, J.-S. Bae, E. Jeong, M.-S. Kwon, J. Yun, D. Choi. Smooth, chemically altered nucleating platform for abrupt performance enhancement of ultrathin Cu-layer-based transparent electrodes. *Nano Letters* **23**, 6528 (2023**)**
5. M. Li, M.T. Curnan, M.A. Gresh-Sill, S.D. House, W.A. Saidi, J.C. Yang, Unusual layer-by-layer growth of epitaxial oxide islands during Cu oxidation. *Nature Communications* **12**, 2781 (2021).
6. M. Mayyas, H. Li, P. Kumar, M. B. Ghasemian, J. Yang, Y. Wang, D. J. Lawes, J. Han, M. G. Saborio, J. Tang, R. Jalili, S. H. Lee, W. K. Seong, S. P. Russo, D. Esrafilzadeh, T. Daeneke, R. B. Kaner, R. S. Ruoff, K. Kalantar-Zadeh, Liquid-metal-templated synthesis of 2D graphitic materials at room temperature. *Advanced Materials* **32**, 2001997 (2020)
7. Y. Chen *et al.*, Cooperative catalysis coupling photo-/photothermal effect to drive Sabatier reaction with unprecedented conversion and selectivity. *Joule* **5**, 3235–3251 (2021)
8. J. Jones *et al.*, Thermally stable single-atom platinum-on-ceria catalysts via atom trapping. Science 353, 150–154 (2016).
9. R. T. Hannagan *et al.*, First-principles design of a single-atom-alloy propane dehydrogenation catalyst. *Science* **372**, 1444–1447 (2021)
10. L. Zeng *et al.*, Stable anchoring of single rhodium atoms by indium in zeolite alkane dehydrogenation catalysts. *Science* **383**, 998–1004 (2024).
11. W. Wan *et al.*, Highly stable and reactive platinum single atoms on oxygen plasma-functionalized CeO_2 surfaces: nanostructuring and peroxo effects. *Angewandte Chemie International Edition* **61**, e202112640 (2022)
12. B. Hu *et al.*, Distinct crystal-facet-dependent behaviors for single-atom palladium-on-ceria catalysts: enhanced stabilization and catalytic properties. *Advanced Materials* **34**, 2107721 (2022).
13. R. Lang *et al.*, Non defect-stabilized thermally stable single-atom catalyst. *Nature Communications* **10**, 234 (2019)
14. M. Peng *et al.*, Antisintering Pd_1 catalyst for propane direct dehydrogenation with in situ active sites regeneration ability. *ACS Catalysis* **12**, 2244–2252 (2022).
15. P. Yin *et al.*, Sulfur stabilizing metal nanoclusters on carbon at high temperatures. *Nature Communications* **12**, 3135 (2021)
16. Y. Nakaya *et al.*, High-entropy intermetallics serve ultrastable single-atom Pt for propane dehydrogenation. *Journal of the American Chemical Society* **144**, 15944–15953 (2022)
17. L. He *et al.*, Robust and coke-free Ni catalyst stabilized by 1–2 nm-thick multielement oxide for methane dry reforming. *ACS Catalysis* **11**, 12409–12416 (2021)
18. F. Talebkeikhah, S. Sun, J. S. Luterbacher, Sinter-resistant nickel catalyst for lignin hydrogenolysis achieved by liquid phase atomic layer deposition of alumina. *Advanced Energy Materials* **13**, 2203377 (2023)
19. S. Li *et al.*, Unusual facet-dependent sintering in Pd-TiO_2 catalysts revealed by theory and experiment. *ACS Catalysis* **14**, 1608-1619 (2024)